The set-down and set-up of directionally spread and crossing surface gravity wave groups

J. Fluid Mech. (2018), *vol.* 835, *pp.* 131–169.

doi:10.1017/jfm.2017.774

The set-down and set-up of directionally spread and crossing surface gravity wave groups

M. L. McAllister[1], T. A. A. Adcock[2], P. H. Taylor[2,3] and T. S. van den Bremer[1,†]

[1]School of Engineering, University of Edinburgh, Edinburgh EH9 3FB, UK

[2]Department of Engineering Science, University of Oxford, Oxford OX1 3PJ, UK

[3]Faculty of Engineering, Computing and Mathematics, University of Western Australia, Crawley WA 6009, Australia

(Received 18 May 2017; revised 26 August 2017; accepted 19 October 2017)

For sufficiently directionally spread surface gravity wave groups, the set-down of the wave-averaged free surface, first described by Longuet-Higgins and Stewart (*J. Fluid Mech.* vol. 13, 1962, pp. 481–504), can turn into a set-up. Using a multiple-scale expansion for two crossing wave groups, we examine the structure and magnitude of this wave-averaged set-up, which is part of a crossing wave pattern that behaves as a modulated partial standing wave: in space, it consists of a rapidly varying standing-wave pattern slowly modulated by the product of the envelopes of the two groups; in time, it grows and decays on the slow time scale associated with the translation of the groups. Whether this crossing wave pattern actually enhances the surface elevation at the point of focus depends on the phases of the linear wave groups, unlike the set-down, which is always negative and inherits the spatial structure of the underlying envelope(s). We present detailed laboratory measurements of the wave-averaged free surface, examining both single wave groups, varying the degree of spreading from small to very large, and the interaction between two wave groups, varying both the degree of spreading and the crossing angle between the groups. In both cases, we find good agreement between the experiments, our simple expressions for the set-down and set-up, and existing second-order theory based on the component-by-component interaction of individual waves with different frequencies and directions. We predict and observe a set-up for wave groups with a Gaussian angular amplitude distribution with standard deviations of above 30–40° (21–28° for energy spectra), which is relatively large for realistic sea states, and for crossing sea states with angles of separation of 50–70° and above, which are known to occur in the ocean.

Key words: waves/free-surface flows, surface gravity waves

† Email address for correspondence: ton.vandenbremer@ed.ac.uk

1. Introduction

In order to satisfy the nonlinear kinematic and dynamic free-surface boundary conditions, linear freely propagating surface gravity waves are accompanied by nonlinear bound components. For periodic waves, a so-called Stokes expansion in the amplitude of the waves reveals that any periodic wave is accompanied by a series of harmonic components with integer multiples of the frequency of the linear parent wave and their magnitude proportional to increasing integer powers of the steepness (Stokes 1847). For multichromatic parent waves representing wave groups, the harmonic components interact to give both 'frequency-sum' and 'frequency-difference' terms, as first described by Longuet-Higgins & Stewart (1962) for unidirectional waves and to second order in steepness. Although expressions for the frequency-difference terms in a multidirectional sea can be distilled from Hasselmann (1962) (cf. Okihiro, Guza & Seymour 1992), Sharma & Dean (1981), Dalzell (1999) and Forristall (2000) are commonly credited for extending the work of Longuet-Higgins & Stewart (1962) to directional seas, allowing for interactions between parent wave components of different frequencies and travelling in different directions (see Pellet *et al.* (2017) for a recent rederivation that also includes pressure). In the limit of a quasimonochromatic group with a single carrier wave travelling in one direction, differential equations describing these second-order bound interactions can also be calculated using a multiple-scale approach. In the seminal papers by Dysthe (1979) (infinite water depth) and Davey & Stewartson (1974) (finite water depth), the nonlinear evolution equations for the wave group are accompanied by a second set of differential equations describing the mean flow and the wave-averaged free surface.

Physically, in the unidirectional case, the bound frequency-difference terms cause a depression in the wave-averaged surface elevation on the scale of the wave group, often referred to as a set-down (Longuet-Higgins & Stewart 1962). It can be thought of as the free-surface manifestation of the return flow underneath the group that forms to balance the Stokes transport, which is divergent on the scale of the group and acts to 'pump' fluid from its trailing edge to its leading edge (McIntyre 1981; van den Bremer & Taylor 2015, 2016). In the classical interpretation, the return flow is driven by a gradient in the radiation stresses (Longuet-Higgins & Stewart 1964). The set-down is simply largest at the centre of the group, where the (negative) return flow is also largest in magnitude. In the limit of a unidirectional deep-water parent wave and a group that is long relative to the water depth d, the set-down becomes (Longuet-Higgins & Stewart 1964)

$$\eta_{-}^{(2)} = -\frac{|A(\tilde{x})|^2}{4d}, \tag{1.1}$$

where A denotes the amplitude envelope of the group and $\tilde{x} = x - c_{g,0}t$ is the horizontal coordinate in the group reference frame. We will briefly review the derivation of (1.1) in § 2.

However, when examining the very large freak wave that occurred at the Draupner Platform in the North Sea on 1 January 1995, Walker, Taylor & Eatock Taylor (2004) observed a large set-up in the wave-averaged surface elevation. Subsequent analysis of the Draupner wave by Adcock & Taylor (2009) and Adcock *et al.* (2011) identified crossing waves as the probable cause of the set-up associated with the Draupner wave. This finding is supported by a high-resolution hindcast model of the Draupner storm performed by Cavaleri *et al.* (2016), which highlighted the presence of two large crossing wave systems. In addition to Draupner, Fedele *et al.* (2016) examined set-up in the wave-averaged surface elevation of two other very large wave

events, concluding that crossing directional spectra were the likely cause. The set-up of the wave-averaged free surface in crossing seas can thus be seen as an important contribution to the crest height of freak waves (see Kharif & Pelinovsky (2003), Dysthe, Müller & Krogstad (2008), Onorato *et al.* (2013) and Adcock & Taylor (2014) for reviews of the mechanisms behind freak waves). We specifically do not examine herein the possible (enhanced) occurrence of modulational or Benjamin–Feir instability in crossing seas, as might be described by coupled nonlinear Schrödinger equations (e.g. Onorato, Osborne & Serio (2006) and references therein).

A set-up was also observed by Toffoli *et al.* (2007) for smaller waves measured on Lake George, Australia. Toffoli *et al.* (2007) showed this effect to be consistent with second-order theory, and found that crossing waves of similar frequency result in positive interaction by numerically computing the frequency-difference interaction kernel of Sharma & Dean (1981). These effects were also observed in time-domain simulations performed by Toffoli, Onorato & Monbaliu (2006). A similar observation was made by Okihiro *et al.* (1992) based on the (equivalent) frequency-difference interaction kernel reconstructed from Hasselmann (1962), noting that this kernel reduces with increasing angle and changes sign for two wave components at an angle of 30° in deep water ($k_0 d \gg 1$). Indeed, the energy spectrum associated with second-order bound waves reduces considerably with increasing directional spreading (Herbers, Elgar & Guza 1994). Recently, Herbers & Janssen (2016) have shown that the set-down associated with (unidirectional) groups can appear as a significant set-up in Lagrangian buoy records, emphasizing the need to carefully distinguish between Lagrangian and Eulerian field observations.

Experimentally, Johannessen & Swan (2001) examined the evolution and focusing of moderately directionally spread focused wave groups and found that the directionality of the wave groups serves to reduce the overall nonlinearity of the waves, affecting the onset of breaking and nonlinear modification of the free waves. Onorato *et al.* (2009) and Toffoli *et al.* (2010) performed experiments and numerical analysis of irregular crossing waves, observing a direct relationship between crossing angle and kurtosis, an indicator of the probability of freak wave occurrence. All of the experimental studies that we are aware of have been limited to small degrees of directional spreading and have not observed the formation of a set-up, with the exception of Toffoli *et al.* (2011), who did conduct experiments with crossing wave systems at crossing angles up to 40°, but did not specifically examine the occurrence of a set-up.

Herein, we examine the structure and magnitude of the wave-averaged free surface for directionally spread and crossing surface gravity wave groups through a combination of multiple-scale expansions and physical experiments for all possible degrees of spreading. We investigate when a set-down can turn into a set-up. Our experiments are conducted in the circular wave tank at the FloWave Ocean Energy Research Facility at the University of Edinburgh (see Ingram *et al.* (2014) for details of the facility). This has 168 individually controlled paddles, enabling the generation of wave groups with any desired directional distribution. We carry out two categories of experiments: tests in which we vary the degree of directional spreading for an individual wave group (category A) and tests in which we let two wave groups cross each other at different angles (category B). Figure 1 illustrates the linear surface profile at the time of linear focus for the groups we examine experimentally in category A, showing specifically three individual groups of increasing degree of directional spreading. Figure 2 shows the perfectly focused predicted linear surface profile for two groups with narrow individual degrees of directional spreading crossing at an angle, as examined in category B.

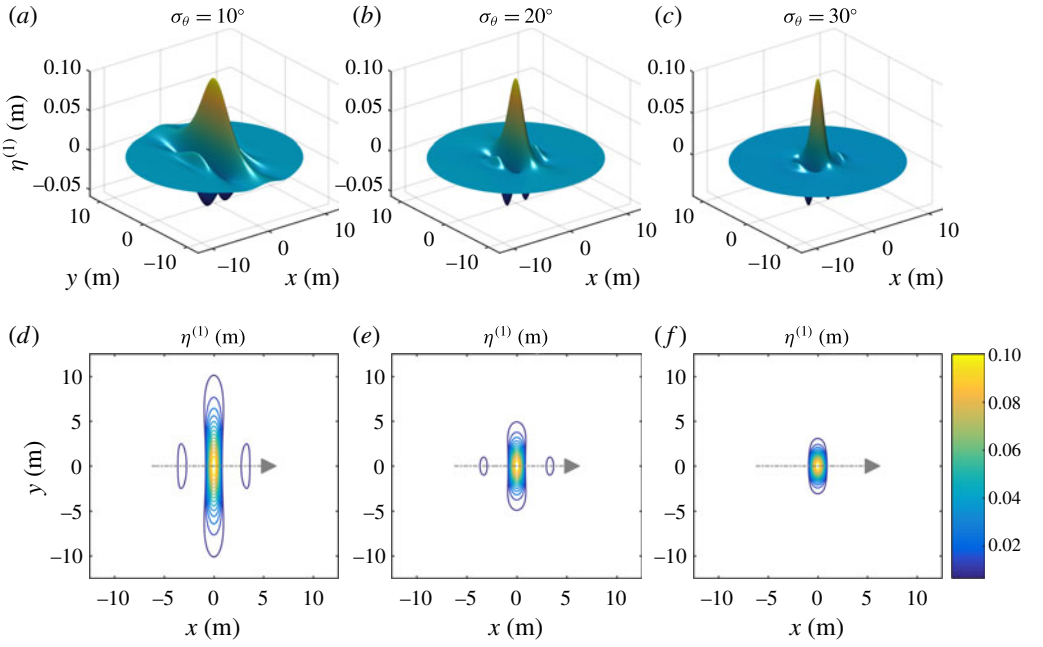

FIGURE 1. (Colour online) Illustration of the linear surface profile $\eta^{(1)}(x, y, t = 0)$ for spreading and surface tests (category A) at time of focus ($t = 0$) and for three different degrees of spreading, $\sigma_\theta = 10, 20, 30°$. (*a–c*) The surfaces and (*d–f*) the corresponding contours, showing positive contours only for clarity (linear amplitude at focus $a_0 = 0.1$ m for a perfectly focused linear group). The colour bar applies to (*d–f*) only.

This paper is laid out as follows. First, in § 2, we present our multiple-scale solutions for crossing groups and review existing second-order theory. In § 3, we outline our experimental method and introduce the two types of experiments we perform. We compare our experimental results with theory in § 4. Finally, conclusions are drawn in § 5.

2. Second-order theory

In this section, we use a multiple-scale approach to gain insight into the mechanisms behind the formation of the set-down or set-up of the wave-averaged free surface and their relative magnitudes under different circumstances. We begin by briefly reviewing the governing equations and boundary conditions in § 2.1, followed by a discussion of the set-down formed for a single narrowly spread group in § 2.2 and the formation of a set-up when two groups cross each other at an angle in § 2.3. Finally, in § 2.4, we compare our simple expressions for the set-down and set-up with the explicitly computed wave-averaged free-surface elevation from existing second-order theory based on the component-by-component interaction of individual waves with different frequencies and directions.

2.1. *Governing equations*

A three-dimensional body of water of depth d and indefinite lateral extent is assumed with a coordinate system (x, y, z), where x and y denote the horizontal coordinates

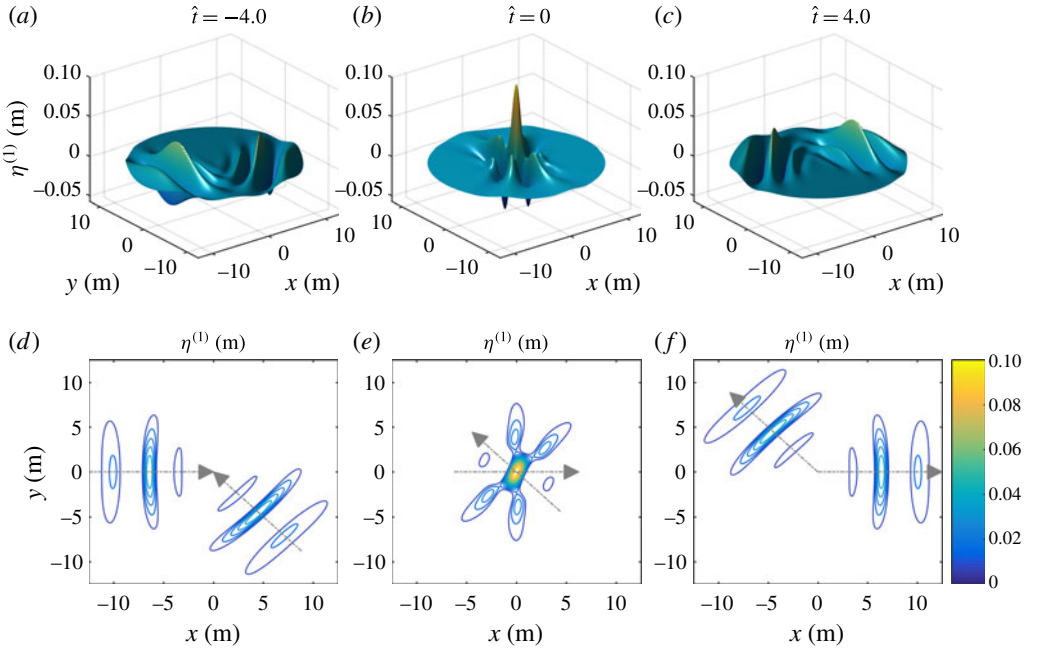

FIGURE 2. (Colour online) Illustration of the linear surface profile $\eta^{(1)}(x, y, t)$ for crossing tests (category B), showing two wave groups with moderate degrees of directional spreading ($\sigma_\theta = 10°$) at a crossing angle of $\Delta\theta = 135°$ for three different times, $\hat{t} \equiv c_{g,0}t/\sigma_x$: before focus at $\hat{t} = -4.0$ (*a*,*d*), at linear focus $\hat{t} = 0$ (*b*,*e*) and after focus at $\hat{t} = 4.0$ (*c*,*f*); (*a–c*) display the linear surfaces and (*d–f*) the corresponding contours, showing positive contours only for clarity (combined linear amplitude at focus $a_0 = 0.1$ m). The colour bar applies to (*d–f*) only.

and z the vertical coordinate measured from the undisturbed water level upwards. Inviscid, incompressible and irrotational flow is assumed and, as a result, the velocity vector can be defined as the gradient of the velocity potential, $\boldsymbol{u} = \nabla\phi$. The governing equation within the domain of the fluid is then Laplace,

$$\nabla^2\phi = 0 \quad \text{for} \quad -d \leqslant z \leqslant \eta(x, y, t), \tag{2.1}$$

where $\eta(x, y, t)$ denotes the free surface. The kinematic and dynamic free-surface boundary conditions are respectively

$$w - \frac{\partial\eta}{\partial t} - u\frac{\partial\eta}{\partial x} - v\frac{\partial\eta}{\partial y} = 0, \quad g\eta + \frac{\partial\phi}{\partial t} + \frac{1}{2}|\nabla\phi|^2 = 0 \quad \text{at } z = \eta(x, y, t), \tag{2.2a,b}$$

where gravity g acts in the negative z direction and $|\nabla\phi|^2 = u^2 + v^2 + w^2$. Finally, there is a no-flow bottom boundary condition, requiring that $\partial\phi/\partial z = 0$ at $z = -d$. By retaining terms up to quadratic in the amplitude of the waves, the two free-surface boundary conditions in (2.2) can be combined into two forcing equations for the mean flow and the wave-averaged free surface respectively,

$$\left(\frac{\partial}{\partial z} + \frac{1}{g}\frac{\partial^2}{\partial t^2}\right)\phi^{(2)}_-\Big|_{z=0} = \overline{\nabla_H \cdot (\boldsymbol{u}^{(1)}_H|_{z=0}\eta^{(1)}) - \frac{1}{g}\frac{\partial}{\partial t}\left(\frac{\partial^2\phi^{(1)}}{\partial z\partial t}\Big|_{z=0}\eta^{(1)} + \frac{1}{2}|\nabla\phi|^2_{z=0}\right)}, \tag{2.3}$$

$$\eta_-^{(2)} = \frac{-1}{g}\left(\left.\frac{\partial \phi_-^{(2)}}{\partial t}\right|_{z=0} + \overline{\left(\left.\frac{\partial^2 \phi^{(1)}}{\partial z \partial t}\right|_{z=0}\eta^{(1)} + \frac{1}{2}|\nabla\phi|^2\Big|_{z=0}\right)}\right), \tag{2.4}$$

where the superscripts denote the order in amplitude and the subscripts signify that we only retain wave-averaged terms here, as also indicated by the overlines on the right-hand side. We specify our definition of wave-averaging below. Finally, the subscript H denotes horizontal components only, so that $\boldsymbol{u}_H = (u, v, 0)$.

2.2. *A single narrow-banded and narrowly spread wave group: set-down*

We first consider a single wave group travelling in the positive x direction, which has the linear signal

$$\eta^{(1)} = Re[A(X, Y)\mathrm{e}^{\mathrm{i}(k_0 x - \omega_0 t)}], \quad \phi^{(1)} = Re\left[-\mathrm{i}\frac{\omega_0}{k_0}A(X, Y)\mathrm{e}^{k_0 z + \mathrm{i}(k_0 x - \omega_0 t)}\right], \tag{2.5a,b}$$

where we have assumed that the linear wave is short relative to the water depth, so that $k_0 d \gg 1$, as in the rest of this paper and for the experiments we perform. We will refer to this assumption as deep water, although the water depth is not truly infinite, and, in fact, it is shallow to intermediate relative to the spatial extent of the group. The linear dispersion relationship becomes $\omega_0^2 = gk_0$, and the prefactor on $\phi^{(1)}$ has been chosen so that the linearized boundary conditions (2.2) are satisfied. To leading-order in the multiple-scale parameter $\epsilon_x \equiv 1/(k_0\sigma_x)$, with σ_x denoting the characteristic spatial scale of the group in its direction of propagation, the group is a function of the slow variables, $X \equiv \epsilon_x(x - c_{g,0}t)$ and $Y \equiv \epsilon_y y$, where $c_{g,0} = \mathrm{d}\omega_0/\mathrm{d}k_0 = \omega_0/(2k_0)$ is the group velocity. We define $\epsilon_y \equiv 1/(k_0\sigma_y)$ and set $O(\epsilon_y) = O(\epsilon_x)$ or smaller. The case $\epsilon_y = \epsilon_x$ corresponds to a round envelope ($\sigma_y = \sigma_x$) and $\epsilon_y \to 0$ to a long-crested or unidirectional wave group. By transforming into the reference frame of the group, neglecting the higher-order (in ϵ_x) double time derivative on the left-hand side of (2.3) and substituting the linear solutions (2.5) on the right-hand side, the mean flow forcing equation (2.3) becomes, after averaging over the fast temporal scales (cf. Dysthe 1979),

$$\left.\frac{\partial \phi_-^{(2)}}{\partial z}\right|_{z=0} = \frac{1}{2}\omega_0 \epsilon_x \partial_X |A|^2, \tag{2.6}$$

where only the divergence of the Stokes transport $\overline{\nabla_H \cdot (\boldsymbol{u}_H^{(1)}(z=0)\eta^{(1)})}$ on the right-hand side of (2.3) contributes for deep water ($k_0 d \gg 1$), and a small degree of directional spreading is captured by the slow variation of the envelope in the direction normal to propagation (Y). For quasimonochromatic wave groups, the problem is steady, and the return flow is simply the irrotational and incompressible response to the divergence of the Stokes transport (cf. 'Stokes pumping') in the reference frame of the group, as is well known (see van den Bremer & Taylor (2016) for a discussion of the generally small effects of dispersion and a comparison of the multiple-scale solution with the original solution of Longuet-Higgins & Stewart (1962)). Solution of the Laplace equation $\nabla^2 \phi_-^{(2)} = 0$, subject to the bottom boundary condition and the forcing equation (2.6) in Fourier space, gives after averaging over the fast temporal scales (cf. van den Bremer & Taylor 2015)

$$\phi_-^{(2)} = \frac{\mathrm{i}\omega_0 |a_0|^2 \sigma_x \sigma_y}{8\pi}\int_{-\infty}^{\infty}\int_{-\infty}^{\infty}\frac{\kappa \cosh(\sqrt{\kappa^2+\lambda^2}(z+d))}{\sqrt{\kappa^2+\lambda^2}\sinh(\sqrt{\kappa^2+\lambda^2}d)}\mathrm{e}^{-(\kappa\sigma_x)^2/4-(\lambda\sigma_y)^2/4}\mathrm{e}^{\mathrm{i}(\kappa\tilde{x}+\lambda\tilde{y})}\,\mathrm{d}\kappa\,\mathrm{d}\lambda, \tag{2.7}$$

where we have chosen a Gaussian envelope, $A = a_0 \exp(-\tilde{x}^2/(2\sigma_x^2) - \tilde{y}^2/(2\sigma_y^2))$, with $\tilde{x} = x - c_{g,0}t$ and $\tilde{y} = y$, for illustrative purposes. Turning to the wave-averaged surface forcing equation (2.4), it can be shown by substituting the linear solutions (2.5) on the right-hand side that, for a single wave group in deep water ($k_0 d \gg 1$), only the mean flow term $(-(1/g)\partial\phi_-^{(2)}/\partial t)$ makes a non-zero contribution. Transforming into the group reference frame and substituting (2.7), equation (2.4) becomes

$$\eta_-^{(2)} = \frac{-|a_0|^2\sigma_x\sigma_y}{16\pi}\int_{-\infty}^{\infty}\int_{-\infty}^{\infty}\frac{\kappa^2}{\sqrt{\kappa^2+\lambda^2}\tanh(\sqrt{\kappa^2+\lambda^2}d)}\mathrm{e}^{-(\kappa\sigma_x)^2/4-(\lambda\sigma_y)^2/4}\mathrm{e}^{\mathrm{i}(\kappa\tilde{x}+\lambda\tilde{y})}\,\mathrm{d}\kappa\,\mathrm{d}\lambda. \tag{2.8}$$

If we further assume $d/\sigma_x \ll 1$, namely that the return flow is shallow, equation (2.8) simplifies to

$$\eta_-^{(2)} = \frac{-|a_0|^2\sigma_x\sigma_y}{16\pi d}\int_{-\infty}^{\infty}\int_{-\infty}^{\infty}\frac{\kappa^2}{\kappa^2+\lambda^2}\mathrm{e}^{-(\kappa\sigma_x)^2/4-(\lambda\sigma_y)^2/4}\mathrm{e}^{\mathrm{i}(\kappa\tilde{x}+\lambda\tilde{y})}\,\mathrm{d}\kappa\,\mathrm{d}\lambda. \tag{2.9}$$

In the limit of a long-crested or unidirectional wave group $R \equiv \sigma_x/\sigma_y \to 0$, we can recover (1.1), which in turn corresponds to the well-known result by Longuet-Higgins & Stewart (1964) (equation (16), p. 549) derived by considering horizontal gradients in radiation stresses. It is evident that, in this limit ($R \to 0$ and $d/\sigma_x \ll 1$), the wave-averaged set-down inherits the spatial structure and shape of the wave group envelope, but with opposite sign. For a non-shallow return flow ($d/\sigma_x = O(1)$), the set-down is accompanied by two positive humps in front and behind, as is evident from the black lines in figure 3(*a*). For directionally spread groups, these humps are generally larger and the set-down is less deep, as is illustrated by comparing either the continuous ($d/\sigma_x = O(1)$) or the dashed ($d/\sigma_x \to 0$) lines in this figure. For arbitrary wave group aspect ratio, the integral (2.9) can be explicitly evaluated at the centre of the group,

$$\eta_-^{(2)}(\tilde{x}=0, \hat{y}=0) = \frac{-|a_0|^2}{4d}\frac{1}{1+R}, \quad \text{with } R \equiv \frac{\sigma_x}{\sigma_y}. \tag{2.10}$$

It is evident then from (2.10) that the magnitude of the set-down of the wave-averaged free surface reduces for more directionally spread groups. This results from a reduction of the magnitude of return flow straight underneath the group, as the response to the 'Stokes pumping' can now not only return below, but also around the group. Figure 3(*b*) illustrates the aspect ratio of the wave-averaged set-down, defined as $R_{SD} \equiv \sigma_x/\sigma_{y,SD}$, with $\sigma_{y,SD}$ computed explicitly as the square root of the second central moment of area of the wave-averaged free surface in the y direction (at $x = 0$) and σ_x still defined as a property of the group. Showing R_{SD} as a function of the aspect ratio of the group itself, $R = \sigma_x/\sigma_y$, figure 3(*b*) demonstrates that the set-down is generally wider than the group, a phenomenon more generally known as 'remote recoil' in wave–mean-flow interaction theory (Bühler & McIntyre 2003).

2.3. *Two crossing groups: set-up and set-down*

We now consider two quasimonochromatic wave groups that cross at $x = y = 0$ (at $t = 0$): group 1 with envelope A_1 travelling in the positive x direction and group 2 with envelope A_2 travelling at an angle $\Delta\theta$ from group 1, with $\Delta\theta$ measured anticlockwise from the positive x-axis. For simplicity, we assume that the two groups are entirely

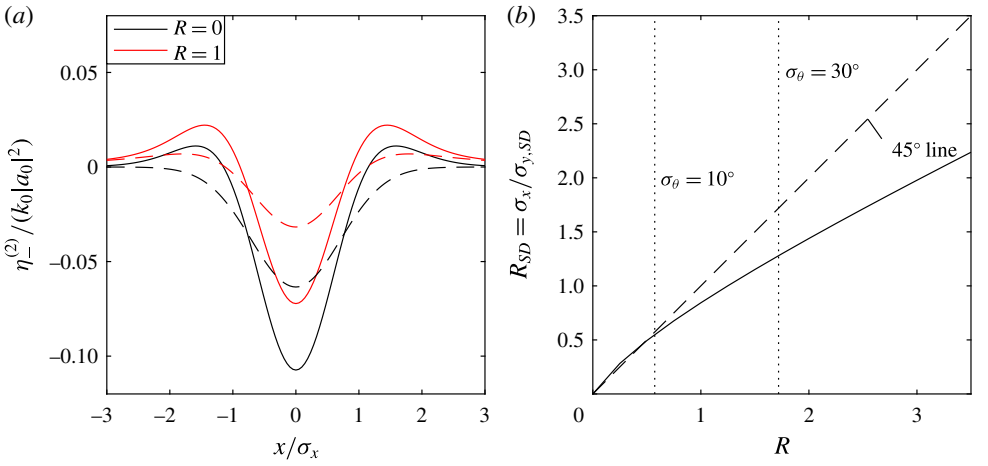

FIGURE 3. (Colour online) Theoretical aspects of the wave-averaged free surface for a single group: (*a*) set-down profile for a single wave group, showing the set-down for $d/\sigma_x = 1.2 = O(1)$ (continuous lines) and in the shallow return flow limit $d/\sigma_x \to 0$ (dashed lines), and (*b*) aspect ratio of the wave-averaged free surface, R_{SD}, as a function of the aspect ratio of the group, $R \equiv \sigma_x/\sigma_y$. We set $\epsilon_x = 0.30$, corresponding to experiments.

equivalent with the exception of their amplitudes and directions of travel, and have for the linear surface elevation

$$\eta^{(1)} = Re[A_1(X_1, Y_1)\mathrm{e}^{\mathrm{i}(k_0 x - \omega_0 t)} + A_2(X_2, Y_2)\mathrm{e}^{\mathrm{i}(k_0 x\cos(\Delta\theta) + k_0 y\sin(\Delta\theta) - \omega_0 t)}], \tag{2.11}$$

where group 1 is a function of the slow scales $X_1 = \epsilon_x(x - c_{g,0}t)$ and $Y_1 = \epsilon_y y$ and group 2 of $X_2 = \epsilon_x(x\cos(\Delta\theta) + y\sin(\Delta\theta) - c_{g,0}t)$ and $Y_2 = \epsilon_y(-x\sin(\Delta\theta) + y\cos(\Delta\theta))$, so that X_1 and X_2 are in the direction of propagation of their respective groups. Substitution of (2.11) and its velocity potential counterpart $\phi^{(1)}$ into the mean flow forcing equation (2.3) gives after some manipulation and to leading-order in the multiple-scale parameter ϵ_x

$$\left.\frac{\partial \phi_-^{(2)}}{\partial z}\right|_{z=0} = \underbrace{F_{A1A1} + F_{A2A2} + F_{A1A2}}_{\equiv\ F}, \tag{2.12}$$

where the forcing is provided by the divergence of the Stokes transport of group 1 with envelope $A_1 = |A_1|\exp(\mathrm{i}\mu_1)$ (F_{A1A1}), group 2 with envelope $A_2 = |A_1|\exp(\mathrm{i}\mu_2)$ (F_{A2A2}) and their interaction (F_{A1A2}),

$$\left.\begin{aligned} F_{A1A1} &= \tfrac{1}{2}\omega_0\epsilon_x\partial_{X_1}|A_1|^2, \\ F_{A2A2} &= \tfrac{1}{2}\omega_0\epsilon_x\partial_{X_2}|A_2|^2, \\ F_{A1A2} &= \frac{1}{2}\omega_0\left(\frac{\epsilon_x(1+3\cos(\Delta\theta))}{2}(|A_1|_{X_1}|A_2| + |A_1||A_2|_{X_2})\right. \\ &\quad \left. + \epsilon_y\sin(\Delta\theta)(|A_1|_{Y_1}|A_2| - |A_1||A_2|_{Y_2})\right) \\ &\quad \times \cos(k_0 x(1-\cos(\Delta\theta)) - k_0 y\sin(\Delta\theta) + \mu_1 - \mu_2). \end{aligned}\right\} \tag{2.13a–c}$$

The phases of the two groups are denoted by μ_1 and μ_2, and we have averaged over the fast temporal scales. The forcing and its response are no longer steady. Avoiding the prohibitively cumbersome Fourier transforms of F_{A1A2}, we immediately assume that the return flow is shallow ($d/\sigma_x \ll 1$), so that we can solve the two-dimensional Laplace equation subject to a distribution of sources and sinks of fluid given by (2.12)–(2.13) in physical space,

$$\phi_-^{(2)}(x, y, t) = -\frac{1}{4\pi d}\int_{-\infty}^{\infty}\int_{-\infty}^{\infty} F(x^*, y^*, t)\log((x-x^*)^2+(y-y^*)^2)\,\mathrm{d}x^*\,\mathrm{d}y^*. \tag{2.14}$$

It can readily be shown that for $\Delta\theta = 0$, equation (2.14) reduces to the mean flow of a single group (2.7) with $A = A_1 + A_2$. Turning to its forcing equation (2.4), we decompose the wave-averaged surface elevation into a set-down η_{SD} and an additional term, which we will later see arises because of wave crossing and we will term the crossing wave (CW) contribution η_{CW},

$$\eta_-^{(2)} = \underbrace{\eta_{SD,A1A1} + \eta_{SD,A2A2} + \eta_{SD,A1A2}}_{=\eta_{SD}} + \eta_{CW}. \tag{2.15}$$

The set-down arises purely in response to the return flow (i.e. through $-(1/g)\partial\phi_-^{(2)}/\partial t$ in (2.4)) and can be decomposed into three terms corresponding to the three forcing terms in (2.13). Corresponding to F_{A1A1}, we have after transforming into the reference frame of group 1

$$\eta_{SD,A1A1}(\tilde{x}_1, \tilde{y}_1) = \frac{|a_1|^2}{4d}\frac{1}{\pi\sigma_x^2}\int_{-\infty}^{\infty}\int_{-\infty}^{\infty}\frac{\mathrm{e}^{-(\tilde{x}_1^*)^2/\sigma_x^2-(\tilde{y}_1^*)^2/\sigma_y^2}\tilde{x}_1^*(\tilde{x}_1-\tilde{x}_1^*)}{(\tilde{x}_1-\tilde{x}_1^*)^2+(\tilde{y}_1-\tilde{y}_1^*)^2}\,\mathrm{d}\tilde{x}_1^*\,\mathrm{d}\tilde{y}_1^*, \tag{2.16}$$

where we have assumed a Gaussian envelope as before, namely $A_1 = a_1\exp(-\tilde{x}_1^2/(2\sigma_x^2) - \tilde{y}_1^2/(2\sigma_y^2))$, with $a_1 = |a_1|\exp(\mathrm{i}\mu_1)$, $\tilde{x}_1 = x - c_{g,0}t$ and $\tilde{y}_1 = y$. By replacing $(\tilde{x}_1, \tilde{y}_1)$ with $(\tilde{x}_2, \tilde{y}_2)$ and $|a_1|^2$ with $|a_2|^2$, we can find an equivalent expression for the set-down $\eta_{SD,A2A2}$ associated with group 2. Although the set-downs for the two individual groups are steady in their respective reference frames, their interaction is unsteady, and we have

$$\eta_{SD,A1A2}(\tilde{x}, \tilde{y}) = \frac{1}{4d}\frac{1}{\pi}\int_{-\infty}^{\infty}\int_{-\infty}^{\infty}\frac{1}{g}\frac{\partial F_{A1A2}(x^*, y^*, t)}{\partial t}\log((x-x^*)^2+(y-y^*)^2)\,\mathrm{d}x^*\,\mathrm{d}y^*, \tag{2.17}$$

where the forcing can be obtained by differentiating F_{A1A2} in (2.13*c*) with respect to time,

$$\begin{aligned}\frac{1}{g}\frac{\partial F_{A1A2}}{\partial t} = &-\frac{|A_1||A_2|}{4\sigma_x^2}\left(\frac{1+3\cos(\Delta\theta)}{2}\left(\frac{(\tilde{x}_1+\tilde{x}_2)^2}{\sigma_x^2}-2\right)\right.\\ &\left.+\sin(\Delta\theta)\frac{(x\sin(\Delta\theta)+y(1-\cos(\Delta\theta)))(\tilde{x}_1+\tilde{x}_2)}{\sigma_y^2}\right)\\ &\times\cos(k_0x(1-\cos(\Delta\theta))-k_0y\sin(\Delta\theta)+\mu_1-\mu_2),\end{aligned} \tag{2.18}$$

where we use a mixture of coordinate systems for notational convenience. Apart from the set-down terms, the two terms on the right-hand side of (2.4) give rise to an

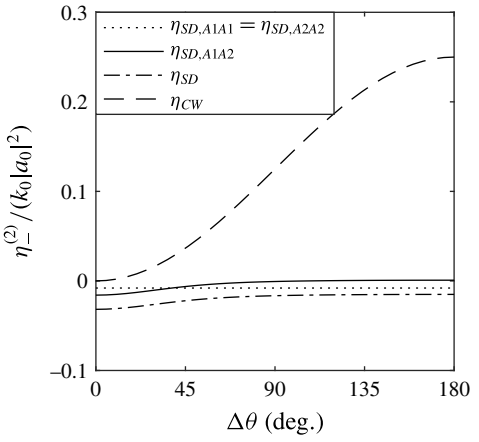

FIGURE 4. The different contributions to the total wave-averaged free surface at the focus point and time as a function of the crossing angle $\Delta\theta$ for two in-phase ($\mu_1 = \mu_2 = 0$) round ($R = 1$) wave groups ($\epsilon_x = 0.30$ and $d/\sigma_x = 1.2$).

additional term, after averaging over the fast temporal scales, which is responsible for the set-up, but is inherently associated with crossing waves,

$$\begin{aligned}\eta_{CW} &= \frac{-1}{g}\overline{\left(\frac{\partial^2\phi^{(1)}}{\partial z\partial t}\bigg|_{z=0}\eta^{(1)} + \frac{1}{2}|\nabla\phi|^2\bigg|_{z=0}\right)} \\ &= \frac{1}{2}(1-\cos(\Delta\theta))k_0|A_1||A_2| \\ &\quad\times \cos(k_0(\underbrace{x(1-\cos(\Delta\theta)) - y\sin(\Delta\theta)}_{=\tilde{x}_1-\tilde{x}_2}) + \mu_1 - \mu_2). \end{aligned} \tag{2.19}$$

We note that, although the set-down is always slowly varying in both time and space, the crossing wave contribution (2.19) responsible for the set-up is slowly varying in time but rapidly varying in space. A partial standing-wave pattern forms with lines of constant phase at an angle $\Delta\theta/2$ to the x-axis, namely in line with the bisection of the paths of travel of the two groups. The pattern varies rapidly in space, and is slowly modulated in time and space by the product of the amplitude envelopes of the two groups (see figure 6*i–l*). Whether η_{CW} is actually manifested as a set-up of the wave-averaged free surface at the location of linear focus ($x = y = 0$) depends trivially on the relative phases of the two groups ($\mu_1 - \mu_2$). The presence of a set-up is thus an indicator of perfect or near-perfect focusing of the underlying linear signal ($\mu_1 = \mu_2$). It is noteworthy that (provided that $k_0 d \gg 1$) the magnitude of the wave crossing contribution is not a function of the magnitude of the depth relative to the scale of the group, unlike the set-down, which decreases in magnitude with increasing d/σ_x. Finally, it is worth noting that the partial standing wave that forms the set-up does not have a counterpart in the second-order velocity field, unlike the set-down.

In time, the behaviour of the wave-averaged free surface as the two groups cross is as follows: the groups are accompanied by a set-down before and after crossing; at the time of crossing, the wave-averaged free surface consists of a wave-group-like structure itself with a set-up at the focus location for the phases $\mu_1 = \mu_2$. Figure 4 shows the magnitudes of the different terms that compose the total wave-average

surface in (2.15) as a function of $\Delta\theta$. The self-interaction term $\eta_{SD,A1A1}$ remains constant and negative, as it is independent of the interaction of the two groups, and similarly for $\eta_{SD,A2A2}$. The cross-interaction set-down term $\eta_{SD,A1A2}$ is initially negative and reduces to zero at $\Delta\theta = 180°$. The set-down associated with two groups that collide head-on is simply equal to the sum of their respective set-downs, $\eta_{SD} = \eta_{SD,A1A1} + \eta_{SD,A2A2}$. Finally, the crossing wave term η_{CW} is zero for $\Delta\theta = 0$, as in this limit the solution reduces to that of a single group. For $\Delta\theta \to 180°$, the crossing wave term increases to a maximum, as can also be readily concluded from inspection of (2.19).

Summarizing results, the behaviour of the wave-averaged free surface is driven by two distinct physical processes, the first of which can only give rise to a set-down and the second of which takes the form of a modulated partial standing-wave pattern and may or may not give rise to a set-up. The set-down forms as the simple free-surface manifestation of the Eulerian return flow that forms underneath a group in response to the divergence of the Stokes transport on the group scale. The set-down can be computed directly from the unsteady Bernoulli equation, retaining the unsteady potential corresponding to the return flow (and ignoring all other terms). The magnitude of the set-down reduces with increasing directional spreading, as the return flow can flow around as well as underneath the group and reduces in magnitude. The set-down does not form for periodic waves; it depends on the group structure. Although its magnitude does not depend on the group width in the limit in which the group width is larger relative to the water depth, it generally reduces with increasing group width. When two groups (or indeed two periodic waves) cross at an angle, further terms in the Bernoulli equation, which are zero for deep water and for a single group or a crossing angle of zero degrees, give rise to a partial standing-wave pattern. Its magnitude does not depend on the group width or on the water depth, provided that $k_0 d \gg 1$. The standing-wave pattern is fixed in space and is modulated by the product of the two groups in both space and time. A set-up forms at the point of focus and crossing, if the two groups are in phase, so that their amplitudes are both positive there.

2.4. *Multicomponent second-order theory (review)*

The expressions for the wave-averaged free-surface elevation derived thus far have relied on two approximations: the spectrum is narrow-banded in both frequency and direction, so that the group can be modelled using the leading-order terms in a multiple-scale expansion. By considering the linear signal as the sum of individual components with different frequencies travelling in different directions, Hasselmann (1962) implicitly and, much later yet explicitly, Sharma & Dean (1981), Dalzell (1999) and Forristall (2000) derived interaction kernels for the nonlinear bound harmonics at second order. We assume independence between the directional Ω and amplitude $\hat{\eta}$ distributions, so that the linear signal is given by a summation over N_k discrete components in N_θ directions,

$$\eta^{(1)} = \sum_{n=1}^{N_k} \sum_{i=1}^{N_\theta} \Omega(\theta_i)\hat{\eta}_n \cos(\varphi_{n,i})\delta k \delta\theta, \quad \text{with } \varphi_{n,i} = \boldsymbol{k}_{n,i} \cdot \boldsymbol{x} - \omega_n t + \mu_n, \tag{2.20}$$

where the wavenumber vector $\boldsymbol{k}_{n,i} = k_n(\cos(\theta_i), \sin(\theta_i))$ has magnitude k_n and θ is measured anticlockwise from the positive x-axis. Every component satisfies the linear dispersion relationship $\omega_n^2 = g k_n \tanh(k_n d)$, where $\tanh(kd) \approx 1$ for almost all

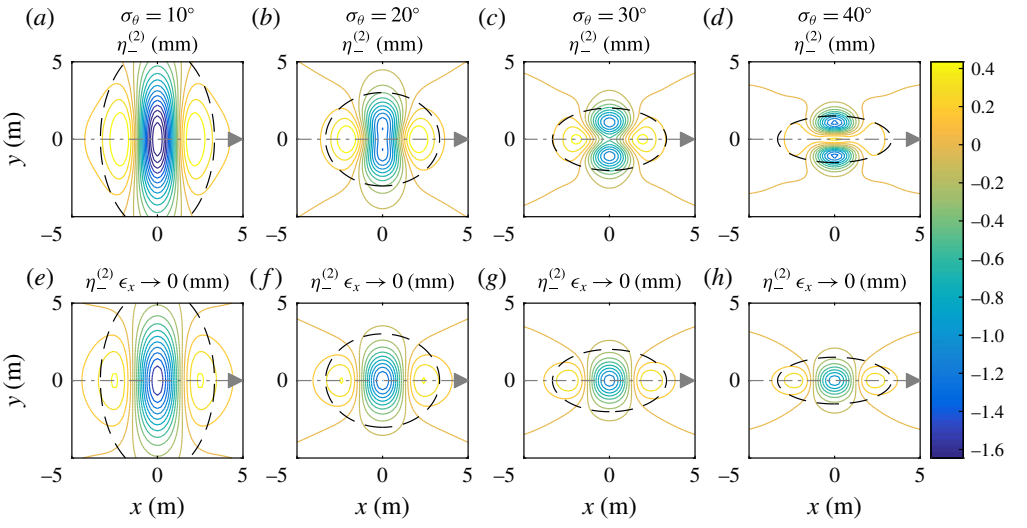

FIGURE 5. (Colour online) Contours of the wave-averaged surface elevation $\eta_-^{(2)}$ for a single group at time of linear focus for different degrees of spreading σ_θ; (*a–d*) are computed from multicomponent second-order theory (2.21) and (*e–h*) correspond to the quasimonochromatic limit (2.8), as denoted by $\epsilon_x \to 0$. The aspect ratio in the quasimonochromatic limit is computed from $R = \sigma_\theta/\epsilon_x$, which is asymptotically valid in the limit of a small degree of spreading ($R = 0.6,\ 1.1,\ 1.7,\ 2.3$ for the four values of σ_θ respectively). The black dashed lines correspond to two standard deviations from the centre of the group.

components of the linear spectrum in our experiments. The coefficients δk and $\delta\theta$ correspond to the magnitude of the discrete steps, so that $\delta k \to \mathrm{d}k$ as $N_k \to \infty$ and similarly for $\delta\theta$. The corresponding second-order difference waves that represent the wave-averaged free surface may be calculated as (Dalzell 1999)

$$\eta_-^{(2)} = \sum_{n=1}^{N_k}\sum_{m=1}^{N_k}\sum_{i=1}^{N_\theta}\sum_{j=1}^{N_\theta} \Omega(\theta_i)\Omega(\theta_j)\hat{\eta}_n\hat{\eta}_m B^-(\boldsymbol{k}_{n,i}, \boldsymbol{k}_{m,j}, \omega_n, \omega_m, d)\cos(\varphi_{n,i} - \varphi_{m,j})(\delta k)^2(\delta\theta)^2, \tag{2.21}$$

where the interaction kernel B^- is given in appendix A.

For the experimental parameters considered herein ($\alpha = k_0 a_0 = 0.20$, $\epsilon_x = 1/(k_0\sigma_x) = 0.30$, $k_0 d = 3.9$ and $d/\sigma_x = 1.2$), discussed in more detail in § 3, figure 5 compares the component-by-component solution (2.21) (*a–d*) with the multiple-scale solution for the set-down (2.8) (*e–h*) for a single wave group, demonstrating good agreement for low degrees of spreading. The mean direction of wave group propagation is left to right in the positive x direction. For high degrees of spreading, a set-up starts to appear in the form of a ridge along the x-axis that connects the humps in front of and behind the group and that is not predicted by the multiple-scale solution (2.8).

Figure 6 compares the component-by-component solution (2.21) (*a–d*) for two crossing groups at four different crossing angles with the multiple-scale solution (2.15) (*m–p*). Also shown are the individual contributions from the set-down (2.16)–(2.17) in (*e*)–(*h*) and the crossing wave pattern (2.19) in (*i*)–(*l*). It is evident from this comparison that the multiple-scale solution can predict the magnitude, but not the exact spatial structure, of the set-down for $\Delta\theta = 45°$, as the directional spectra of

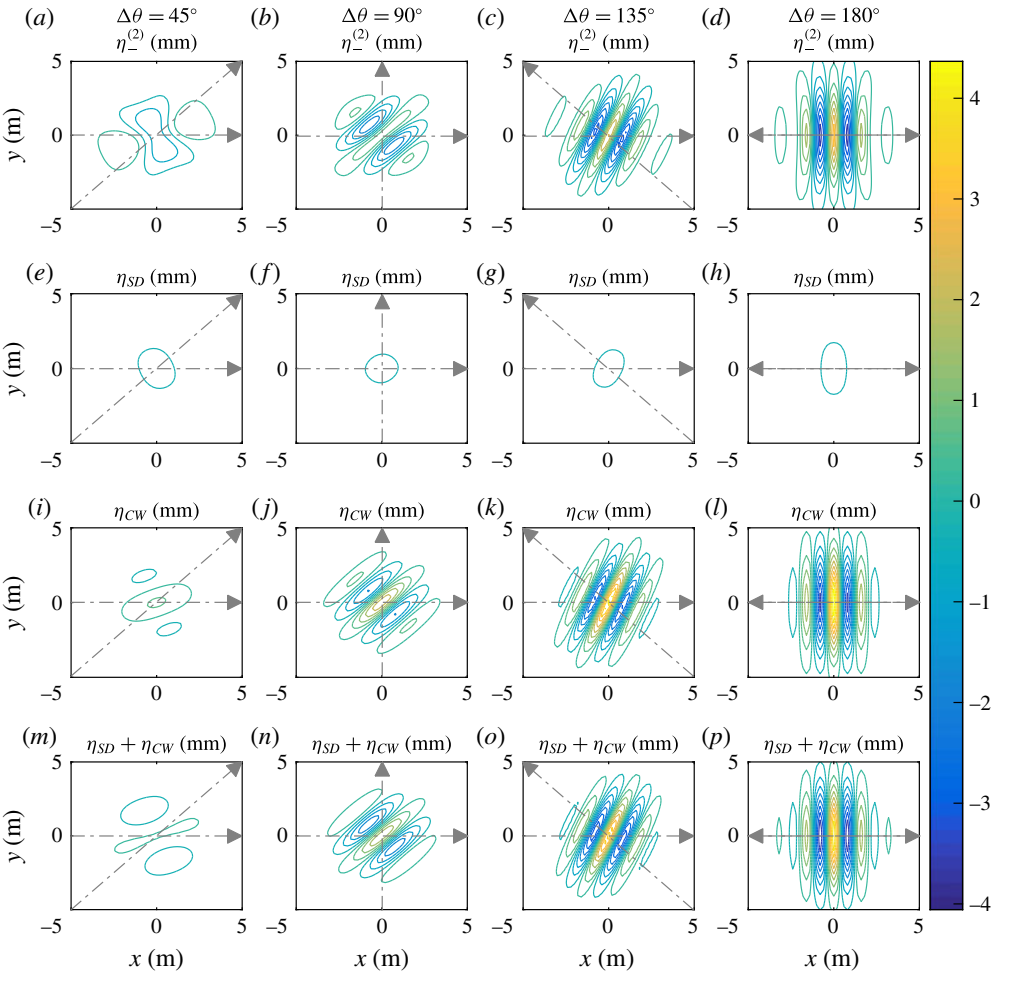

FIGURE 6. (Colour online) Contours of the wave-averaged surface elevation $\eta_-^{(2)}$ for crossing wave groups at time of linear focus for different crossing angles $\Delta\theta$; (*a–d*) are computed from multicomponent second-order theory (2.21), (*e–h*) correspond to the set-down in the quasimonochromatic limit (2.16)–(2.17), (*i–l*) correspond to the crossing wave pattern in the quasimonochromatic limit (2.19) and (*m–p*) correspond to the sum of the last two. The degree of spreading of the individual groups is $\sigma_\theta = 10°$.

the group are not clearly separated for low crossing angles. For all larger crossing angles, the two methods agree well, and the set-up is dominant.

3. Experimental method

This section introduces the experimental set-up (§ 3.1), details the input parameters of each category of experiment (§ 3.2) and introduces the method used to isolate the wave-averaged surface elevation from the measured signal (§ 3.3). Sections 3.4 and 3.5 respectively describe our estimation of spectral and directional parameters from the measured signal. Finally, § 3.6 discusses sources of measurement error and repeatability.

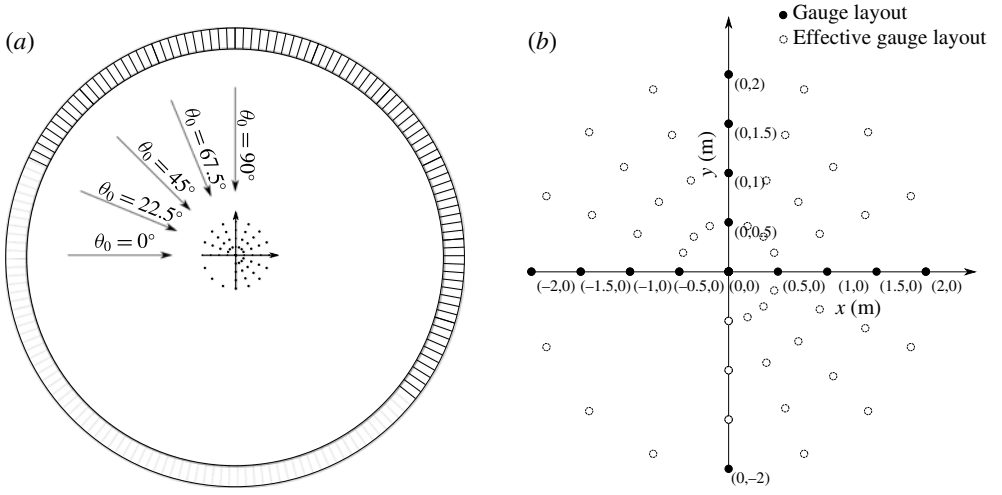

FIGURE 7. The gauge array layout, showing wave gauge locations with respect to the centre of the tank ($x = 0$, $y = 0$). The closed circles denote the location of the 14 gauges with the positive x-axis corresponding to the mean direction of travel of the group (or one of the groups). The open circles denote the effective gauge layout achieved by changing the mean wave direction in steps of 22.5° to map out the wave-averaged free surface. The arrows in (*a*) illustrate the mean direction of each repeated test used to achieve this.

3.1. *FloWave and gauge layout*

The experiments are conducted at the FloWave Ocean Energy Research Facility at the University of Edinburgh. The circular multidirectional wave basin has a 25 m diameter, is 2 m deep and is encircled by 168 actively absorbing force-feedback wavemakers, allowing for the creation of waves in all directions. All of our experiments are of sufficiently short duration, with a run time of 32 s, for reflections not to play a role. The generation of waves by the wavemakers is based on linear theory.

Figure 7 shows the layout of the array, consisting of 14 capacitance wave gauges within the tank, with gauge locations chosen to combine good spatial resolution while being spaced far enough apart to capture the entire spatial structure of the wave-averaged free surface. Practically constrained by a limited number of wave gauges available and their robust positioning on an overhanging gantry, we place all of our wave gauges along the main axis of travel of the group (x-axis) and on the positive half of the orthogonal y-axis (with the exception of one further gauge at negative y), as illustrated by the closed circles in figure 7. To gain additional information on the two-dimensional structure of the free surface, we repeat (a selection of) the same experiments varying their angle of propagation relative to the gauge array, thus obtaining the effective gauge layout illustrated by the open circles in figure 7. These repetitions are carried out at intervals of 22.5° between 0° and 90°, as illustrated by the arrows in figure 7(*a*). The wave gauges are calibrated at the start of each day of testing. A settling time of 10 min between each test is employed to allow for the absorption of reflected waves.

3.2. *Matrix of experiments and input parameters*

We conduct tests in two categories: spreading tests (category A, § 3.2.1) and crossing tests (category B, § 3.2.2), as summarized in table 1. In these two categories of test,

Category	Test numbers	a_0 (m)	σ_θ (deg.)	$\Delta\theta$ (deg.)
A. Spreading	A.1–13	0.1	0–90 (at 10), 135, 180, 360	0
	A.14–19	0.15	0–50 (at 10)	0
B. Crossing	B.1–12	0.1	10, 20, 30	45–180 (at 45)
	B.13–16	0.15	20	45–180 (at 45)
	B.17	0.1	0	180

TABLE 1. Matrix of experiments.

we respectively vary the degree of directional spreading for a single group (A) and consider two crossing groups for different crossing angles (B). For all experiments, we base the input on a Gaussian amplitude distribution in wavenumber magnitude $k = |\boldsymbol{k}|$,

$$\hat{\eta}(k) = \frac{a_0}{\sqrt{2\pi}\Delta k} \exp\left(-\frac{1}{2}\left(\frac{k-k_0}{\Delta k}\right)^2\right) \quad \text{for } 0 \leqslant k \leqslant \infty, \tag{3.1}$$

which is converted into the frequency domain using the linear dispersion relationship before being provided as an input to the wavemakers. We set the peak wavenumber $k_0 = 2.0\ \mathrm{m}^{-1}$ (based on a peak frequency of 0.7 Hz) and adopt a standard deviation of $\Delta k = 0.6\ \mathrm{m}^{-1}$. Although (3.1) only formally corresponds to a group with a Gaussian envelope in real space if k has support on the entire real line (including $k < 0$), $S(k)$ is negligibly small for $k = 0$ and below for the parameters chosen. Thus, $\sigma_x = 1/\Delta k = 1.7$ m corresponds to the spatial scale of the group (the standard deviation of the approximately Gaussian group). We have $\epsilon_x = 0.30$, so the multiple-scale approximation will probably hold, but be associated with an error that scales as ϵ_x^2 ($\sim 10\,\%$). We choose this large value of ϵ_x so that the spatial extent of the group is considerably smaller than that of the tank. This ensures that long second-order error waves associated with the linear paddle motion have time to propagate ahead of the group. Our linear wave is always deep ($k_0 d = 3.9$) and we choose the total linear amplitude a_0 to be 0.1 or 0.15 m, corresponding to a steepness of $\alpha = k_0 a_0 = 0.20$ or 0.30. The steepness of the wave groups is chosen to produce second-order components sufficiently large to observe, while minimizing the effects of higher-order nonlinearity. Wave breaking is not observed during the experiments and is not expected for individual (directionally spread) short groups of such steepness. We consider a Gaussian amplitude distribution in angle θ,

$$\Omega(\theta) = \frac{\Omega_0}{\sqrt{2\pi}\sigma_\theta} \exp\left(-\frac{1}{2}\left(\frac{\theta-\theta_0}{\sigma_\theta}\right)^2\right) \quad \text{for } -180^\circ \leqslant \theta \leqslant 180^\circ, \tag{3.2}$$

where θ_0 is the mean direction and σ_θ is a measure of the degree of directional spreading. We truncate the spreading distribution at -180° and $+180^\circ$ and choose the normalization coefficient Ω_0 so that the sum of $\Omega(\theta)$ is unity over this range. For small degrees of spreading, σ_θ corresponds to the root-mean-squared spreading value. For crossing wave groups, two directional distribution functions with different values of θ_0 are superimposed. We emphasize the difference between our σ_θ and the usual energy spectrum directional spreading parameter, which is equal to $\sigma_\theta/\sqrt{2}$.

3.2.1. *Category A – spreading tests*

First, tests are carried out to assess the relationship between the degree of directional spreading σ_θ, and the amplitude and sign of the wave-averaged surface elevation for a single focused wave group. The degree of directional spreading σ_θ is varied in the range 0–360° for groups with an amplitude of $a_0 = 0.1$ m, and in the range $\sigma_\theta = 0$–50° for an increased amplitude of $a_0 = 0.15$ m. In practice, $\sigma_\theta = 360°$ corresponds to the case where the directional spectrum has almost fully saturated ($\sigma_\theta \to \infty$ corresponds to fully axisymmetric spreading: the variation of $\Omega(\theta)$ as a function of θ is less than 7 % for $\sigma_\theta = 360°$). The difference in the amplitude of the wave-averaged surface elevation between $\sigma_\theta = 360°$ and $\sigma_\theta \to \infty$ is negligible (<0.1 %). An illustration of three of these tests is presented in figure 1 for $\sigma_\theta = 10$, 20, 30°.

Having observed the temporal behaviour of the wave-averaged surface elevation of directionally spread wave groups at the point of intended linear focus, we seek to gain further understanding by measuring the spatial variation of the wave-averaged surface elevation. We achieve this by repeating certain tests and varying the mean direction of propagation relative to the gauge array from 0 to 90° and at intervals of 22.5°. In doing so, we capture the spatial structure of the wave-averaged surface elevation, as measured with the effective gauge layout shown by the open circles in figure 7. We map the wave-averaged free surface by carrying out such repeats for four tests from this category, $\sigma_\theta = 20$, 30, 40° (and at an increased amplitude of $a_0 = 0.15$ m for $\sigma_\theta = 40°$). In doing so, we capture the spatial structure of the wave-averaged free surface dominated by the set-down, the set-up and the transition between these as a function of σ_θ.

3.2.2. *Category B – crossing tests*

Second, tests are carried out to assess the relationship between the crossing angle $\Delta\theta$ of two directionally spread focused wave groups and the set-up or set-down of the wave-averaged surface elevation. The crossing angle $\Delta\theta$ of the wave groups is varied between 0 and 180° at 45° intervals. This is repeated for groups with directional spreading of $\sigma_\theta = 10$, 20, 30° and $a_0 = 0.1$ m (and for an increased amplitude of $a_0 = 0.15$ m at $\sigma_\theta = 20°$). An illustration of one of these tests is presented in figure 2 for $\sigma_\theta = 10°$ and $\Delta\theta = 135°$.

3.3. *Harmonic separation*

In order to observe the wave-averaged free surface of wave groups and other nonlinear harmonics, these components must be extracted from the fully nonlinear signal measured by the gauges. By repeating experiments and changing the phases of all of the linear components of the wave group in the wavemaker signal by 180° between experiments, nonlinear harmonic terms of odd and even powers in amplitude may be extracted from the measured time series (Baldock, Swan & Taylor 1996),

$$\eta_{odd} = \frac{\eta_0 - \eta_{180}}{2}, \quad \eta_{even} = \frac{\eta_0 + \eta_{180}}{2}, \tag{3.3a,b}$$

where η_0 denotes a crest-focused and η_{180} a through-focused repeat of the same experiment. Measured second-order sum $\eta^{(2)}_{M+}$ and difference $\eta^{(2)}_{M-}$ components are then extracted from η_{even} by filtering η_{even} with cutoffs below $1.5\omega_0$ and above $3\omega_0$, and above $0.75\omega_0$ respectively for the reasonably narrow-banded groups considered here. Similarly, the linear signal $\eta^{(1)}_M$ may be extracted from η_{odd}. Carrying out further repeat

experiments with phase shifts of 90° and 270° allows for separation of higher-order harmonics, including for higher-bandwidth signals, in physical experiments (Fitzgerald *et al.* 2014; Mai *et al.* 2016; Zhao *et al.* 2017). We examine these four-phase combinations for spreading tests A.3–4 and A.13 and find that two- and four-phase combinations produce very similar results (see appendix B). Consequently, we repeat all other experiments with only a single phase shift of 180°. It should be noted that the inversion of phase is unaffected by cubic nonlinear interactions, so perfect phase focusing is not required.

3.4. *Estimation of spectral parameters*

As our input amplitude distribution $\hat{\eta}(k)$ is assumed to be Gaussian in wavenumber magnitude, and our measurements are in time, the resulting Fourier transform $\hat{\eta}(\omega)$ is converted in order to estimate spectral parameters by setting $\hat{\eta}(k) = \hat{\eta}(\omega(k))\mathrm{d}\omega(k)/\mathrm{d}k$, where $\omega(k) = \sqrt{kg\tanh kd}$. The carrier wavenumber $k_0^\star$ is estimated as the wavenumber of the spectral peak of the linear spectrum. The linear amplitude $a_0^\star$ is estimated by taking the zeroth moment of the measured linear wavenumber spectrum,

$$a_0^\star = \int_0^\infty \hat{\eta}^{(1)}(k)\,\mathrm{d}k. \tag{3.4}$$

The spectral bandwidth Δk is then estimated using the variance of the observed spectrum,

$$\mathrm{Var}(k) = \frac{1}{a_0^\star}\int_0^\infty \hat{\eta}^{(1)}(k)(k-k_0^\star)^2\,\mathrm{d}k \quad \text{and} \quad \Delta k^\star = \sqrt{\mathrm{Var}(k)}. \tag{3.5a,b}$$

We use the symbol $\star$ throughout to indicate parameters estimated from measurements, as distinct from values provided as inputs to the wavemakers.

3.5. *Estimation of measured directional spectrum*

In all of our experiments, the degree of directional spreading is of primary concern. It is therefore necessary to estimate the actual degree of directional spreading $\sigma_\theta^\star$ experienced for each experiment. The non-ergodic nature of the experiments considered herein makes estimates using maximum-likelihood and entropy methods inappropriate (cf. Krogstad 1988; Benoit, Frigaard & Schäffer 1997). Instead, a least-squares approach is adopted, and $\sigma_\theta^\star$ is identified as the value that minimizes the difference between the measured, $\eta_M^{(1)}$, and predicted, $\eta_T^{(1)}$, linear time series. The predicted time series $\eta_T^{(1)}$ at each probe is calculated using the Fourier transform $\hat{\eta}_M^{(1)}$ of the time series observed at the central probe, which is propagated in space to the other probes using linear wave theory,

$$\eta_T^{(1)}(\boldsymbol{x}_p, t) = Re\left[\sum_{n=1}^{N_k}\sum_{i=1}^{N_\theta} \Omega(\theta_i)\hat{\eta}_{M,n}^{(1)}\exp(-\mathrm{i}(\omega_n t - \boldsymbol{k}_{i,n}\cdot\boldsymbol{x}_p))\delta k\delta\theta\right], \tag{3.6}$$

where $\boldsymbol{x}_p$ is the location of probe p and $\Omega(\theta)$ is the assumed spreading distribution function as a function of the parameter σ_θ to be identified. The least-squares estimate of spreading is then found as

$$\sigma_\theta^\star = \arg\min_{\sigma_\theta}\sum_{p=1}^{N_p}\int_{-6\sigma_x/c_{g,0}}^{6\sigma_x/c_{g,0}} (\eta_M^{(1)}(\boldsymbol{x}_p, t) - \eta_T^{(1)}(\boldsymbol{x}_p, t))^2\,\mathrm{d}t. \tag{3.7}$$

Test:	Input				Estimated			
	σ_θ (deg.)	a_0 (m)	k_0 (m^{-1})	Δk (m^{-1})	$\sigma_\theta^\star$ (deg.)	$a_0^\star$ (m)	$k_0^\star$ (m^{-1})	$\Delta k^\star$ (m^{-1})
A.1	0	0.1	1.97	0.6	0	0.094	1.90	0.56
A.2	10				8.8	0.090	1.74	0.61
A.3†*	20				16.4	0.082	1.74	0.64
A.4†*	30				28.2	0.085	1.90	0.61
A.5†*	40				37.9	0.083	1.90	0.62
A.6	50				47.5	0.081	1.90	0.63
A.7	60				57.0	0.080	1.90	0.64
A.8	70				66.6	0.079	1.90	0.64
A.9	80				76.4	0.078	1.90	0.64
A.10	90				85.9	0.077	1.90	0.65
A.11	135				130.3	0.075	1.90	0.58
A.12	180				178.1	0.076	1.90	0.63
A.13†	360				412	0.076	1.90	0.63
A.14	0	0.15	1.97	0.6	0	0.157	1.74	0.71
A.15	10				7.8	0.138	1.74	0.66
A.16	20				15.7	0.123	1.74	0.65
A.17	30				28.0	0.127	1.90	0.60
A.18*	40				38.0	0.127	1.90	0.61
A.19	50				47.6	0.126	1.90	0.60

TABLE 2. Input and estimated spectral parameters for the spreading tests (category A) († denotes tests that were repeated with additional 90° and 270° phase shifts, and ∗ tests that were repeated with mean direction from 0–90° at intervals of 22.5° to produce spatial measurements).

The integral limits are set to $\pm 6\sigma_x/c_{g,0}$ to capture the passage of the entire wave group, focused at $t = 0$, and minimize the influence of reflections. Our approach assumes that components of equal frequency are in phase at the central probe. This is valid provided that there is not significant modification to the linear dispersion of free waves through cubic wave–wave interactions as the waves travel from the paddles to the observation points.

The input and estimated spectral parameters for each test are presented in tables 2–3 and discussed in § 4.

3.6. *Measurement error and repeatability*

To quantify the sources of error affecting the comparison between our experiments and theory, we examine the role of residual tank motion (error measure I), assess repeatability (error measures II and III), quantify how accurately we can estimate the degree of directional spreading (error measure IV) and, finally, compute the accuracy of wave gauge calibration (error measure V). Details of this error quantification can be found in appendix C, with results summarized in table 4. Looking ahead to the results in § 4, the measured wave-averaged surface elevation is generally in the range ±2 mm for the smaller-amplitude experiments ($a_0 = 0.1$ m) and ±6 mm for the larger-amplitude experiments ($a_0 = 0.15$ m).

We estimate the error in the wave-averaged free surface associated with residual tank motion (error measure I) to be negligibly small (±0.025 mm). The repeatability

	Input					Estimated			
Test:	$\Delta\theta$ (deg.)	σ_θ (deg.)	a_0 (m)	k_0 (m^{-1})	Δk (m^{-1})	$\sigma_\theta^\star$ (deg.)	$a_0^\star$ (m)	$k_0^\star$ (m^{-1})	$\Delta k^\star$ (m^{-1})
B.1	45	10	0.1	1.97	0.6	9.5	0.086	1.90	0.57
B.2	90					9.3	0.086	1.90	0.54
B.3	135					9.7	0.088	1.90	0.58
B.4	180					8.8	0.087	1.90	0.55
B.5	45	20	0.1	1.97	0.6	18.4	0.084	1.90	0.60
B.6	90					18.6	0.082	1.90	0.59
B.7	135					18.5	0.083	1.90	0.58
B.8	180					18.7	0.084	1.90	0.59
B.9	45	30	0.1	1.97	0.6	27.5	0.083	1.90	0.60
B.10	90					28.3	0.083	1.90	0.97
B.11	135					28.2	0.080	1.90	0.61
B.12	180					28.0	0.080	1.90	0.60
B.13	45	20	0.15	1.97	0.6	17.7	0.129	1.96	0.61
B.14	90					18.6	0.127	1.95	0.61
B.15	135					19.1	0.131	1.95	0.61
B.16	180					18.6	0.130	1.88	0.57
B.17†	180	0	0.1	1.97	0.6		—		

TABLE 3. Input and estimated spectral parameters for the crossing tests (category B). The † indicates that test B.17 constituted four separate repeat tests in which unidirectional directional groups were created in phase ($\mu_1 = \mu_2$) and out of phase ($\mu_1 - \mu_2 = 180°$), resulting in total cancellation of the two linear wave groups at $x = 0$ (see figure 15).

of experiments is found be extremely high (error measure II), with exact repeats of the same experiment giving an error in the maximum amplitude of the wave-averaged free surface between repeats of 0.023–0.14 mm. We define our measure of error to be two times the standard deviation in all cases. A more substantial error in the wave-averaged free surface of 0.1–0.38 mm ($a_0 = 0.1$ m) and 0.43 mm ($a_0 = 0.15$ m) (two standard deviations) is identified when the same experiments are repeated, but the main direction of travel of the group is varied, reflecting slight azimuthal asymmetry in the wavemaker configuration or the gauge layout. From repeated resampling from our 14 probes we obtain an error in the wave-averaged free-surface amplitude, resulting from an error in $\sigma_\theta^\star$ of 0.047–0.28 mm ($a_0 = 0.1$ m) and 0.3–0.7 mm ($a_0 = 0.15$ m). Underlying all of these sources of error is most likely the error associated with wave gauge calibration of 0.4 mm (error measure V). As our measures of error are not independent, we take calibration error to be the dominant source of error and use this in the error bars presented in the next section. Specifically, the error bars correspond to two standard deviations either side of the mean.

4. Results

In this section, we compare our experimental results with predictions for the wave-averaged free surface based on the parameters estimated from the linear signal in the two categories we consider: spreading tests (category A, §§ 4.1 and 4.2) and crossing tests (category B, § 4.3). Throughout this section, we compare measured and theoretically predicted surface elevations, denoted by the subscripts M and T

	Description	Test parameters	Test numbers	Error $\pm\Delta\eta_-^{(2)}$ (mm)	Error $\pm\Delta\eta_-^{(2)}/(\lvert a_0^\star\rvert^2 k_0^\star)$
I.	Residual tank motion $\Delta\eta_I$	—	—	0.50	—
	Low-pass filtered $\Delta\eta_I$	—	—	0.025	0.0013
II.	Two standard deviations of the measured wave-averaged surface amplitude $a_{M-}^{(2)}$ from repeated tests $\Delta\eta_{II}$	$\sigma_\theta = 20°$	A.3, A.3†, A.3.1*	0.080	0.0068
		$\sigma_\theta = 30°$	A.4, A.4†, A.4.1*	0.14	0.01
		$\sigma_\theta = 40°$	A.5, A.5†, A.5.1*	0.16	0.012
		$\sigma_\theta = 360°$	A.13, A.13†	0.11	0.01
		$\sigma_\theta = 40°$, $a_0 = 0.15$ m	A.18, A.18.1*	0.023	0.00075
III.	Two standard deviations of the measured wave-averaged surface amplitude $a_{M-}^{(2)}$ from spatial map repeat tests $\Delta\eta_{III}$	$\sigma_\theta = 20°$	A.3.1–A.3.5*	0.38	0.032
		$\sigma_\theta = 30°$	A.4.1–A.4.5*	0.24	0.017
		$\sigma_\theta = 40°$	A.5.1–A.5.5*	0.10	0.0076
		$\sigma_\theta = 40°$, $a_0 = 0.15$ m	A.18.1–A.18.5*	0.43	0.014
IV.	Mean error in $a_{T-}^{(2)}$ associated with estimating $\sigma_\theta^\star$ $\Delta\eta_{IV}$	$a_0 = 0.1$ m	A.1–A.13	0.055	0.0044
		$a_0 = 0.15$ m	A.14–A.19	0.28	0.0086
		$a_0 = 0.1$ m	B.1–B.12	0.047	0.0035
		$a_0 = 0.15$ m	B.13–B.16	0.11	0.0035
V.	Gauge calibration error of central probe (mean $a_0^\star$ and $k_0^\star$ used) $\Delta\eta_V$	—	—	0.4	0.033

TABLE 4. Quantification of errors in the wave-averaged free surface $\eta_-^{(2)}$ († denotes tests that were repeated with additional 90° and 270° phase shifts, and $*$ tests that were repeated in producing spatial measurements).

respectively. The measured wave-averaged surface elevation $\eta^{(2)}_{M-}$ is extracted from the measured time series using the process outlined in § 3.3, and its theoretical counterpart $\eta^{(2)}_{T-}$ is calculated using (2.21), using as inputs the linear part of the time series measured at the central probe, $\eta^{(1)}_{M}$, and the estimated values of $\sigma^{\star}_{\theta}$ reported in tables 2 and 3 for the two respective categories. Appendix D gives the original time series of the free-surface elevation measured at the central probe for completeness.

4.1. *Spreading tests (category A)*

Beginning our discussion with the properties of the linear signal, table 2 compares input and estimated spectral parameters for the spreading tests. The estimated spreading $\sigma^{\star}_{\theta}$ is consistent with the input values of spreading σ_{θ}. A slight offset is observed, with the estimates consistently smaller than the inputs. The increased-amplitude tests A.14–19 show a slightly larger reduction in spreading for tests at $\sigma^{\star}_{\theta} = 10^{\circ}$ and $\sigma^{\star}_{\theta} = 20^{\circ}$, which is consistent with the numerical simulations of Gibbs & Taylor (2005). These authors observe a reduction in spreading proportional to the steepness α^2 for a degree of spreading $\sigma_{\theta} = 15^{\circ}$. Deviations in the amplitude from the input can be attributed to either nonlinear evolution or wavemaker performance. Turning to the estimated wavenumber, we observe a slight reduction in carrier wavenumber for tests with low degrees of directional spreading (0–20°), as evidence of classical down-shift of the peak wavenumber, which is more pronounced for larger steepness (Lake *et al.* 1977; Tian, Perlin & Choi 2011). Consistently, the down-shift becomes less pronounced for increasing degrees of directional spreading, as the effects of spreading serve to decrease the overall degree of nonlinearity (see also Johannessen & Swan 2001). There are no significant trends in the estimated bandwidth $\Delta k^{\star}$.

Figure 8 compares the measured ($\eta^{(2)}_{M-}$) and theoretically predicted ($\eta^{(2)}_{T-}$) wave-averaged surface elevations at the central probe for tests A.1–12. Both the measured and the predicted results show a set-down for low degrees of directional spreading (*a–d*). As the degree of spreading is increased, the amplitude of the set-down decreases, and reaches zero at around $\sigma^{\star}_{\theta} \approx 40^{\circ}$ (*e*), after which a set-up begins to form (*f–l*). The measured and predicted wave-averaged surface elevations show very good agreement, with best agreement for low and high degrees of spreading. At the extremes $\sigma_{\theta} \to 0$ and $\sigma_{\theta} \to \infty$, it is straightforward to accurately estimate the spreading. The slight decrease in agreement for intermediate values of $\sigma^{\star}_{\theta}$ is probably indicative of uncertainty associated with estimation of $\sigma^{\star}_{\theta}$ in this regime. In all cases, the differences between the measured and the predicted values lie well within the approximate error bounds estimated in § 3.6. At higher values of steepness, figure 9 shows improved agreement between the measurements and the predictions in the range $\sigma_{\theta} = 0$–50° (tests A.14–19), especially for intermediate degrees of spreading.

Figure 10 summarizes the results of the spreading tests. Panel (*a*) compares the amplitude of the measured wave-averaged surface elevation $a^{(2)}_{M-}$ with the theoretical prediction $a^{(2)}_{T-}$ calculated from (2.21). The values of $a^{(2)}_{T-}$ in this panel rely on the measured linear spectra, as in figures 8 and 9. Accordingly, we note that the increased-steepness experiments compare with theory slightly better. In order to compute the theoretical line in (*a*), we must specify a single amplitude distribution $\hat{\eta}(k)$, despite slight variations in $k^{\star}_{0}$ and $\Delta k^{\star}$ between experiments (cf. table 2). The red lines in figure 10(*b*) show the amplitude of the wave-averaged surface elevation for a Gaussian amplitude distribution (3.1) with $k_0 = 1.90$ m^{-1} and $\Delta k = 0.60$ m^{-1}. The dotted line, denoted by $\epsilon_x \to 0$, corresponds to the multiple-scale approximation (2.8), whereas the dashed line corresponds to the multiple-component solution (2.21).

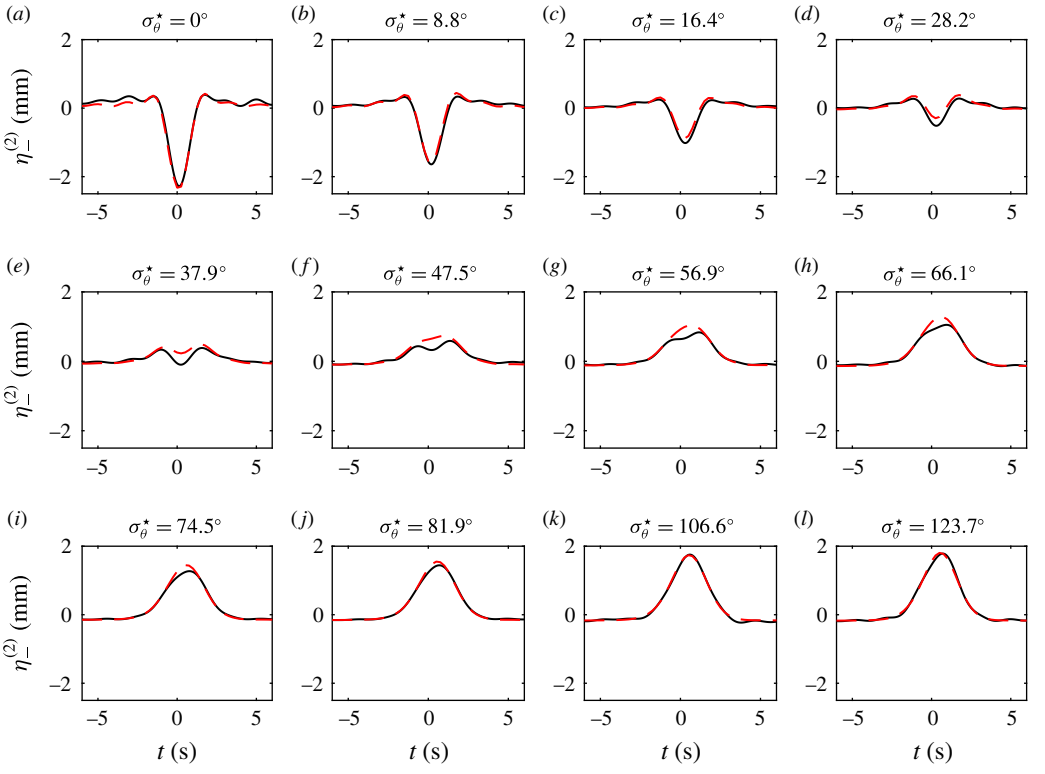

FIGURE 8. (Colour online) The wave-averaged surface elevation $\eta_-^{(2)}$ at the central probe ($x=0$, $y=0$) for the spreading tests (category A), showing measurements $\eta_{M-}^{(2)}$ (black lines) and theoretical predictions $\eta_{T-}^{(2)}$ (red dashed lines) for an input amplitude of $a_0 = 0.1$ m. The different panels correspond to increasing degree of input spreading $\sigma_\theta = 0$–$180°$ (see table 2) and the labels denote the estimated degree of spreading $\sigma_\theta^\star$ used for the theoretical predictions of $\eta_{T-}^{(2)}$.

Both lines rely on the same Gaussian directional distribution. It is evident from comparing these two lines that both approaches agree for small degrees of directional spreading, noting a slight underestimation of the magnitude of the set-down by the multiple-scale approximation ($\epsilon_x = 0.3$). For larger degrees of directional spreading, the multiple-scale solution fails, as expected.

4.2. *Spreading tests (category A): spatial measurements*

Beginning our discussion again with the properties of the linear signal, the estimated spectral parameters for the repeat tests carried out in producing spatial measurements are evidently consistent with those for the analogous tests discussed before (tests A.3–5,18). As we change the direction of travel of the wave group θ_0 from 0 to 90°, leaving the gauge array fixed, we can observe that our estimate of $\sigma_\theta^\star$ varies by 1.2° at most. This variation is less for the increased-amplitude tests, with $\sigma_\theta^\star$ only varying by 0.4°. In order to assess how well the directional spectrum is reproduced by the wavemakers, figure 11 compares the measured linear free surface $\eta_M^{(1)}$ shown in the top half with the predicted linear surface $\eta_T^{(1)}$ at the same gauges mirrored in the bottom

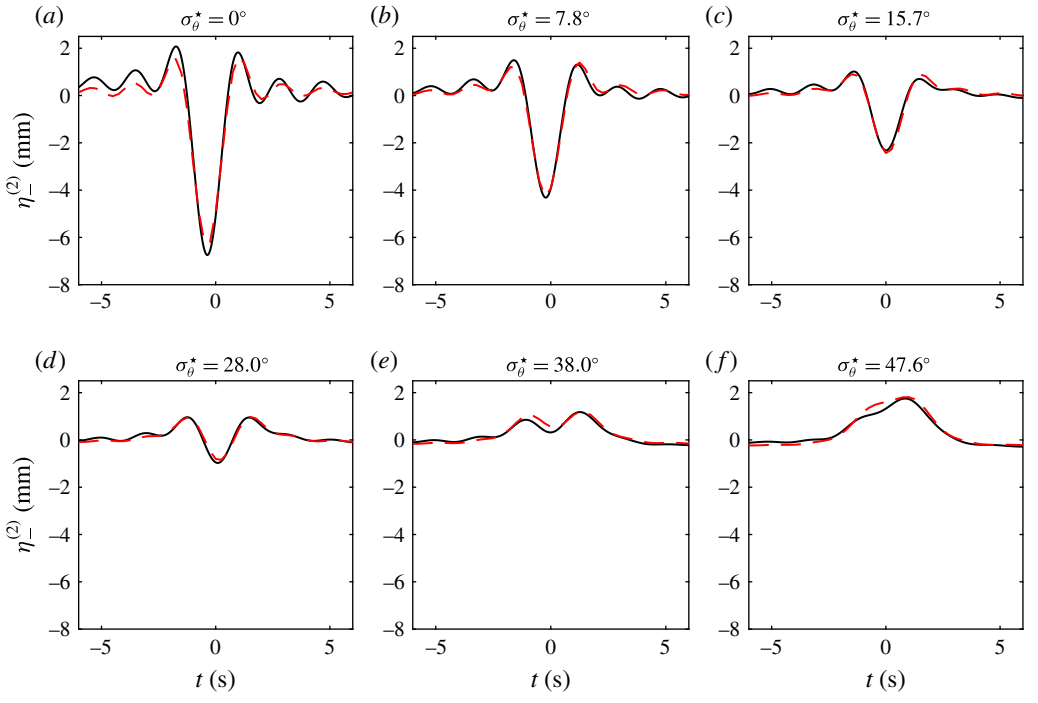

FIGURE 9. (Colour online) The wave-averaged surface elevation $\eta_-^{(2)}$ at the central probe ($x = 0$, $y = 0$) for the spreading tests (category A), showing measurements $\eta_{M-}^{(2)}$ (black lines) and theoretical predictions $\eta_{T-}^{(2)}$ (red dashed lines) for a linear input amplitude of $a_0 = 0.15$ m. The different panels correspond to increasing degree of input spreading $\sigma_\theta =$ 0–50° (see table 2) and the labels denote the estimated degree of spreading $\sigma_\theta^\star$.

half, all at the time of focus. The predicted linear free surface compares very well with measurements, illustrating that our approach is capable of accurately measuring the spatial free-surface elevation and that our estimates of $\sigma_\theta^\star$ are correct.

The two-dimensional structure of the wave-averaged surface elevation is examined in figure 12. Panels (*a–c*) show the measured wave-averaged surface elevation $\eta_{M-}^{(2)}$ as input spreading is increased from 20–40°, and (*d*) shows the increased-amplitude test with $\sigma_\theta = 40°$. For (*a–d*), the measured surface $\eta_{M-}^{(2)}$ in the south-west quadrant ($x < 0$, $y < 0$) is mirrored from the north-west quadrant ($x < 0$, $y > 0$), assuming symmetry, in order to complete the surface measured by our asymmetric gauge array. Panels (*e–h*) show the predicted wave-averaged surface elevation $\eta_{T-}^{(2)}$ (calculated using $\sigma_\theta^\star$). The set-down can clearly be observed as a deep hole that reduces with increasing spreading by the formation of the set-up, eventually splitting into two holes either side of the wave crest, which is now enhanced by a set-up ridge. The agreement is better for the increased-amplitude experiment in (*d*,*h*). For each test, the holes are slightly deeper than predicted and the set-up is slightly less pronounced, all within the bounds of experimental error. The formation of the set-up ridge is clearly captured. It is worth noting that the array of probes used to generate these contours is sparse around the point of focus ($x = 0$, $y = 0$) (see figure 7). Therefore, any error in this area is exaggerated when linear interpolation is used to produce the contour surfaces.

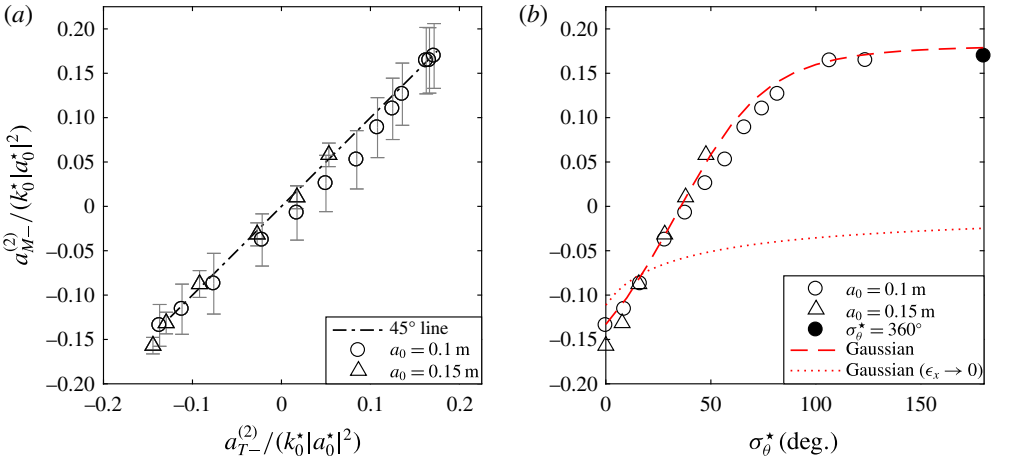

FIGURE 10. (Colour online) The amplitude of the wave-averaged surface elevation at the central probe ($x = 0$, $y = 0$) for the spreading tests (category A); (*a*) shows the measured wave-averaged surface amplitude $a_{M-}^{(2)}$ as a function of the theoretical prediction $a_{T-}^{(2)}$, with error bars shown in grey (see § 3.6 and appendix C for details), and (*b*) shows the measured amplitude $a_{M-}^{(2)}$ as a function of the estimated degree of spreading $\sigma_\theta^\star$. The red dashed lines correspond to a perfectly focused Gaussian wave group.

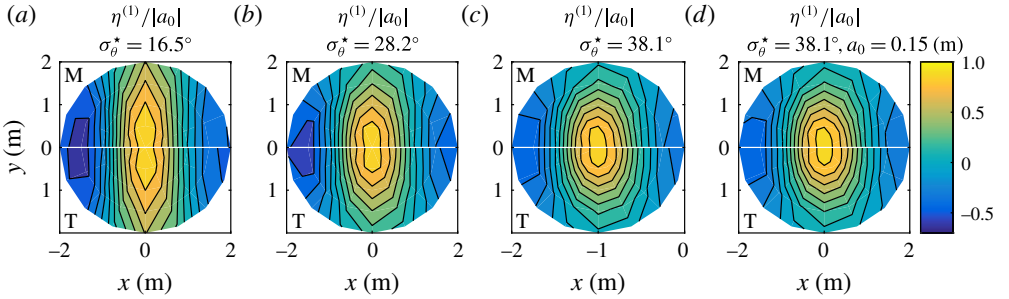

FIGURE 11. (Colour online) Contours comparing the measured linear free surface $\eta_M^{(1)}$ (top half) and the predicted linear surface $\eta_T^{(1)}$ (bottom half) at time of focus; (*a*)–(*c*) correspond to increasing degree of input spreading $\sigma_\theta = 20, 30, 40°$ (for $a_0 = 0.1$ m) and the labels give the estimated degree of spreading $\sigma_\theta^\star$ used for theoretical predictions of $\eta_T^{(1)}$; (*d*) corresponds to an increased amplitude $a_0 = 0.15$ m at $\sigma_\theta = 40°$. Only positive values of y are shown and the white horizontal lines demarcate the measured linear free surface shown in the top half (labelled *M*) and the theoretically predicted linear free surface shown in the bottom half (labelled *T*).

4.3. *Crossing group tests (category B)*

Beginning our discussion with the properties of the linear signal as before, estimated spectral parameters for the crossing tests are reported in table 3. We note that the amplitude refers to the combined linear amplitude of the two groups. As the steepness of the individual groups before they meet is thus halved, this could perhaps explain the reduction in the (small) deviation between input and estimated spreading, and input and estimated carrier wavenumber. Both are associated with nonlinearity, respectively through the phenomena of spectral down-shift and narrowing of the group observed in numerical simulations by Gibbs & Taylor (2005).

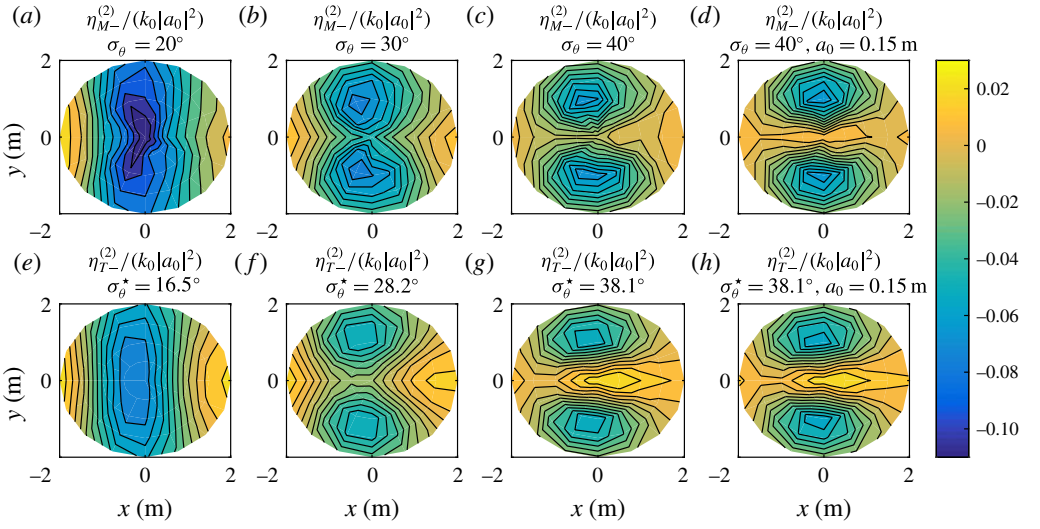

FIGURE 12. (Colour online) Contour plots showing the measured wave-averaged surface elevation $\eta^{(2)}_{M-}$ (*a–d*) and the predicted wave-averaged surface elevation $\eta^{(2)}_{T-}$ (*e–h*) at time of focus; (*a–c*,*e–g*) correspond to increasing degree of input spreading $\sigma_\theta = 20$, 30, 40° (for $a_0 = 0.1$ m) and (*d*,*h*) correspond to an increased amplitude $a_0 = 0.15$ m at $\sigma_\theta = 40°$. The labels in (*e–h*) give the estimated degree of spreading $\sigma^\star_\theta$ used for theoretical predictions of $\eta^{(1)}_T$ (see the supplementary material online available at https://doi.org/10.1017/jfm.2017.774 for animations of $\eta^{(2)}_{M-}(x, y, t)$).

Figure 13 compares the measured ($\eta^{(2)}_{M-}$) and theoretically predicted ($\eta^{(2)}_{T-}$) wave-averaged surface elevations at the central probe for tests B.1–16. For all degrees of spreading and a crossing angle of $\Delta\theta = 45°$, a small set-down is observed. When the crossing angle is increased to 90°, a significant set-up can be observed for all degrees of spreading, growing to a maximum value at a crossing angle of $\Delta\theta = 180°$. The measured and predicted wave-averaged surface elevations again show remarkable agreement, with even better agreement for higher crossing angles.

In the absence of full surface measurements, figure 14 compares measured and theoretical wave-averaged surface elevations along the x-axis, where nine probes are located. There is good agreement between the measurements, $\eta^{(2)}_{M-}$ (black dots), and the multiple-component solution (2.21) (red dashed lines) in all cases. The multiple-scale solution for two crossing groups (2.15) (continuous black lines) is computed under the assumption of perfectly focused Gaussian wave groups ($\mu_1 = \mu_2 = 0$) and is somewhat larger than the multiple-component solution. Nevertheless, the measured wave-averaged surface elevation is well captured by the multiple-scale solution, except for low crossing angles ($\Delta\theta = 45°$), where the azimuthal distribution is not well separated. Crucially, it is evident from figure 14 that for higher crossing angles, all of the wave-averaged surface elevations exhibit a rapidly varying local structure, which differs drastically from the slow hole or hump formed by an individual wave group. As captured by (2.19), the crossing wave pattern consists of a modulated wave group with its peak coinciding with the main linear crest for two wave groups that are in phase ($\mu_1 = \mu_2 = 0$). The set-up crest, in turn, is part of a wider ridge along the bisection of the directions of travel of the two groups.

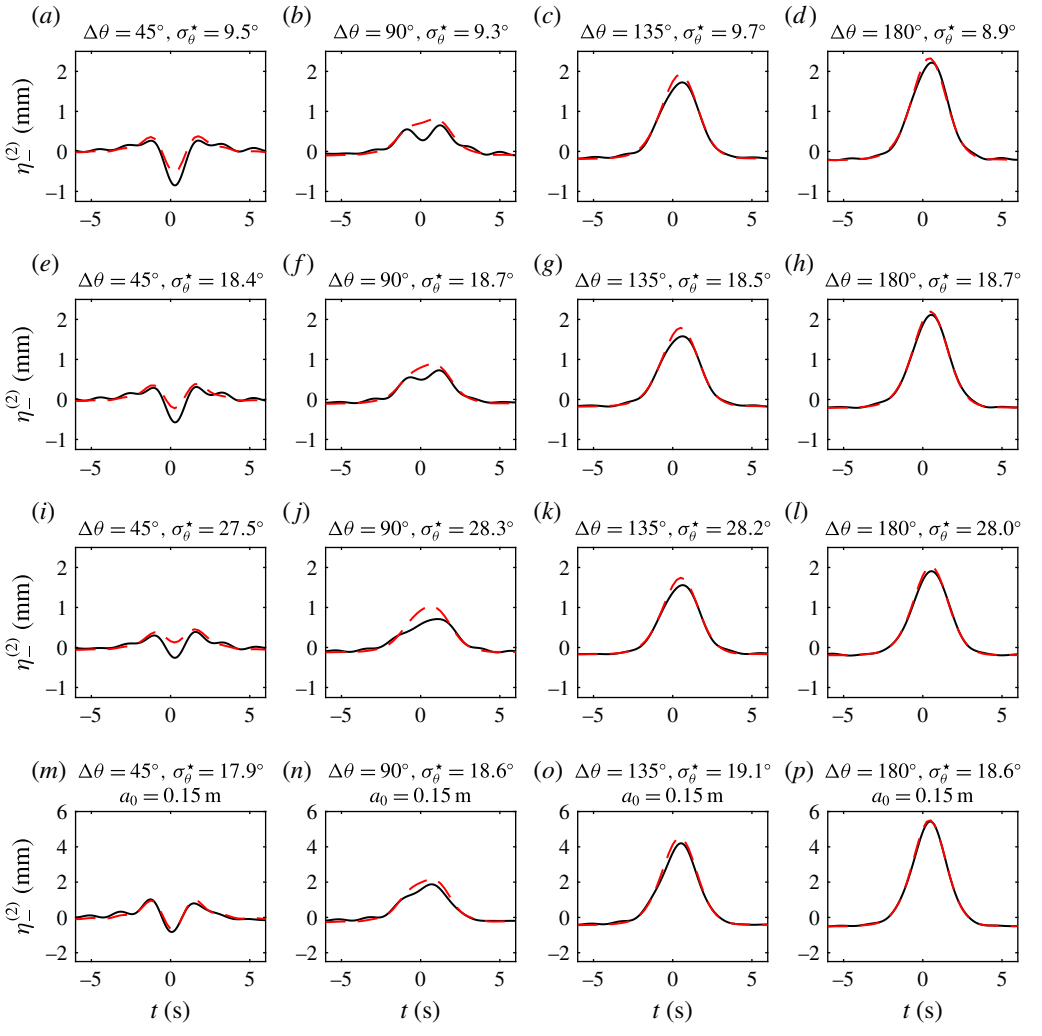

FIGURE 13. (Colour online) The wave-averaged surface elevation $\eta_-^{(2)}$ at the central probe ($x=0$, $y=0$) for the crossing tests (category B), showing measurements $\eta_{M-}^{(2)}$ (black lines) and theoretical predictions $\eta_{T-}^{(2)}$ (red dashed lines) for an input amplitude of $a_0=0.1$ m, for different values of the crossing angle $\Delta\theta=0$–$180°$ and the degree of input spreading $\sigma_\theta=10, 20, 30°$ (*a–d*,*e–h*,*i–l*), with estimated values $\sigma_\theta^\star$ reported in the labels (see table 3); (*m–p*) correspond to increased-amplitude experiments at $a_0=0.15$ m.

4.3.1. *The role of phase*

Examining the role of phase more carefully, figure 15 compares the wave-averaged free surfaces for two opposing unidirectional wave groups ($\Delta\theta=180°$) that are in phase ($\mu_1=\mu_2$) and out of phase ($\mu_1-\mu_2=180°$). When the phase of one group is shifted by 180°, the wave-averaged surface elevation is reversed, becoming negative, as predicted by (2.15). It is also evident from this figure that the 'hole' is deeper than the 'hump', as the set-down is not a function of phase and always remains negative, while the crossing wave contribution changes sign. Nevertheless, it is worth emphasizing that in the in-phase case ($\mu_1=\mu_2$), the linear signal constructively interferes and

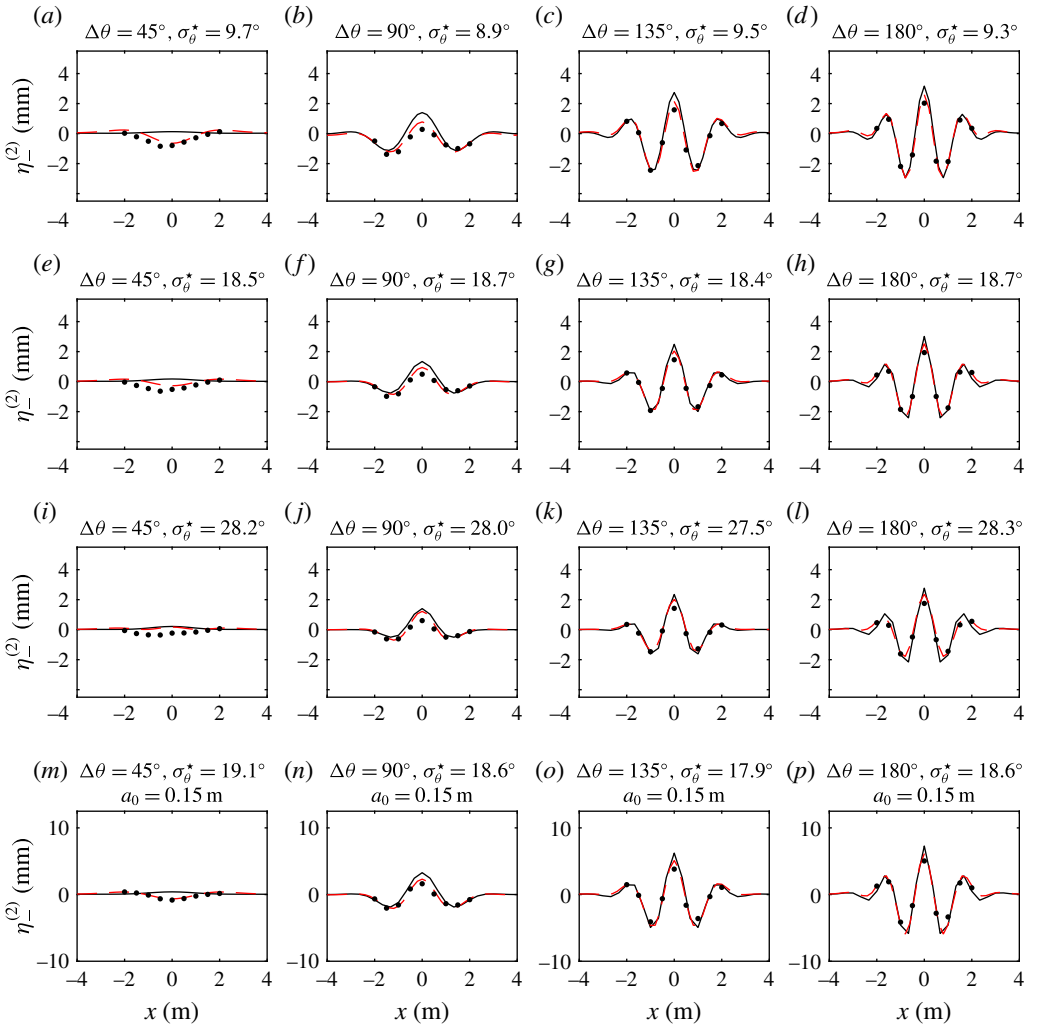

FIGURE 14. (Colour online) The wave-averaged surface elevation $\eta_-^{(2)}$ in the direction of propagation ($y = 0$) at the time of linear focus for the crossing tests (category B), showing measurements $\eta_{M-}^{(2)}$ (black dots), theoretical predictions $\eta_{T-}^{(2)}$ made using the multiple-component solution (2.21) (red dashed lines) and using the multiple-scale solution (2.15) (continuous black lines) for an input amplitude of $a_0 = 0.1$ m, for different values of the crossing angle $\Delta\theta = 0$–$180°$ and the degree of input spreading $\sigma_\theta = 10, 20, 30°$ (*a–d,e–h,i–l*), with estimated values $\sigma_\theta^\star$ reported in the labels; (*m–p*) correspond to increased-amplitude experiments at $a_0 = 0.15$ m.

the 'hump' contributes to an already large and positive crest, whereas in the out-of-phase case ($\mu_1 - \mu_2 = 180°$), the linear signal deconstructively interferes and the 'hole' combined with second-order sum components (see appendix E) is the only observable feature. Finally, due to its (partial) standing-wave nature, the set-up varies slowly in time (*a*), while varying rapidly in space. In time and space, it is subject to the same slow modulation associated with the product of the crossing groups, which travel at twice the group velocity from the perspective of a stationary observer.

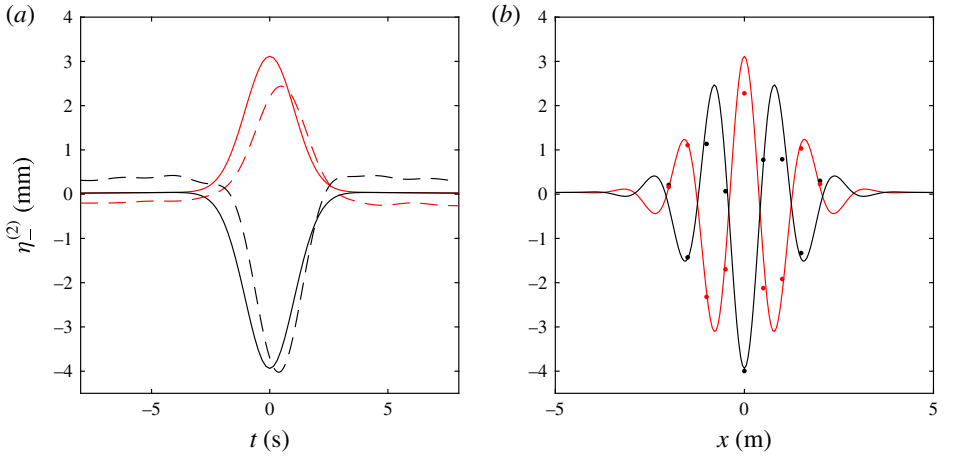

FIGURE 15. (Colour online) Temporal (a) and spatial (b) evolution of the wave-averaged surface elevation $\eta_-^{(2)}$ at the focus point ($x = 0$, $y = 0$) for two wave groups colliding head-on ($\Delta\theta = 180°$). The red lines correspond to two groups that are in phase ($\mu_1 = \mu_2$) and the black lines to groups that are out of phase ($\mu_1 - \mu_2 = 180°$). The multiple-scale solution (2.15) is given by the continuous lines, and the measurements by the dashed lines in (a) and the dots in (b).

Finally, figure 16 summarizes the results of the crossing tests. In (a), the amplitude of the measured wave-averaged surface elevation $a_{M-}^{(2)}$ is shown as a function of the theoretically predicted amplitude $a_{T-}^{(2)}$, showing good agreement. In (b), the amplitude of the measured wave-averaged surface elevation $a_{M-}^{(2)}$ is shown as a function of the crossing angle $\Delta\theta$. As before, in order to compute the theoretical line in (a), we must specify a single amplitude distribution $\hat{\eta}(k)$, despite slight variations in $k_0^\star$ and $\Delta k^\star$ between experiments (cf. table 2). The red dashed lines show the amplitude of the wave-averaged surface elevation for two Gaussian wave groups with $k_0 = 1.90$ m^{-1} and $\Delta k = 0.60$ m^{-1} for degrees of spreading $\sigma_\theta = 10, 20, 30°$.

5. Conclusions

Herein, we have examined the formation of a set-down or set-up of the wave-averaged free surface for compact directionally spread and crossing wave groups on deep water ($k_0 d \gg 1$). We compare detailed measurements conducted at the fully directional FloWave Ocean Energy Research Facility at the University of Edinburgh with existing multiple-component second-order wave theory (Sharma & Dean 1981; Dalzell 1999; Forristall 2000) and derive new results using a multiple-scale approach which lend greater insight into the problem. We believe that ours is the first experimental observation of set-up for highly directionally spread and crossing groups, following field observations of a set-up underneath the famous Draupner rogue wave (Walker *et al.* 2004) and on Lake George, Australia (Toffoli *et al.* 2007).

For a single directionally spread wave group, the total wave-averaged free surface is made up from the combination of a set-down and a set-up, which vary slowly in time but have very different spatial structures. For a perfectly focused wave group and at the centre of the group at the time of focus, the sign of the wave-averaged free surface changes for degrees of directional spreading $\sigma_\theta = 30$–$40°$, which corresponds to more commonly reported degrees of spreading of the energy spectrum of $\sigma_\theta/\sqrt{2} = 21$–$28°$.

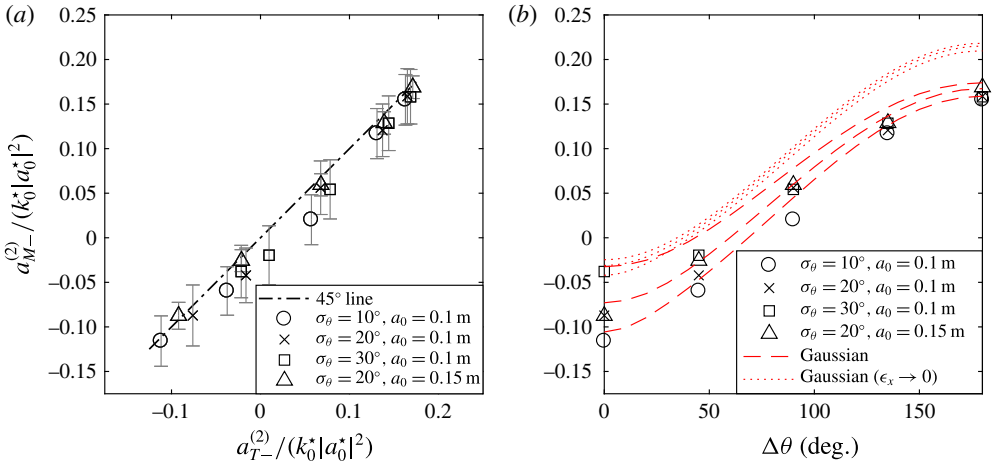

FIGURE 16. (Colour online) The amplitude of the wave-averaged surface elevation at the central probe ($x = 0$, $y = 0$) for the crossing tests (category B). (*a*) The measured wave-averaged surface amplitude $a^{(2)}_{M-}$ as a function of the theoretical prediction $a^{(2)}_{T-}$, with error bars shown in grey (see § 3.6 and appendix C for details). (*b*) The measured amplitude $a^{(2)}_{M-}$ as a function of the crossing angle $\Delta\theta$. The red dashed lines correspond to two perfectly focused crossing Gaussian wave groups with degrees of spreading $\sigma_\theta = 10, 20, 30°$.

The set-down inherits the shape of the group envelope, albeit wider due to the remote recoil of the underlying return flow that causes it, which also occurs for three-dimensional internal wave groups (Bühler & McIntyre 2003). The magnitude of the set-down reduces monotonically with an increasing degree of directional spreading. As the degree of directional spreading increases, the set-up, which is zero for unidirectional seas, forms a ridge through the set-down 'hole' which is aligned in the main direction of propagation of the group. The set-up is in fact part of a crossing wave pattern, which may be modulated by the presence of groups.

The spatial structure of this crossing wave pattern and the associated set-up is elucidated by considering a multiple-scale expansion for two crossing wave groups. It behaves as a partial standing wave. In time, the crossing wave pattern grows and decays on the slow time scale associated with the translation of the groups. In space, it consists of a rapidly varying standing-wave pattern, which is slowly modulated by the product of the envelopes of the two groups. The sign of the crossing wave pattern varies spatially. Whether this crossing wave pattern actually enhances the surface elevation at the point of focus (and leads to a set-up) depends on the phases of the linear wave groups, unlike the set-down, which is always negative and inherits the spatial structure of the underlying envelopes and remains present for crossing groups. If two groups are in phase, the crossing wave ridge formed along the bisection of the two directions of travel is positive, and it is negative for out-of-phase groups. Assuming two groups that are in phase, the total wave-averaged free surface is always positive (a set-up) at the focus location and time for crossing angles of 50–70°, for which the crossing wave contribution dominates.

The practical implications of the change between a set-down to a set-up can be illustrated by considering a large wave group of linear crest height $a_0 = 10$ m, a peak period of 12 s on a water depth of 140 m, representative of realistic severe conditions, and chosen to approximately correspond to the non-dimensional water

depth and steepness in our scaled experiments ($k_0 d = 3.9$, $k_0 a_0 = 0.28$ and $\epsilon_x = 0.3$). For single wave groups with degrees of spreading of $\sigma_\theta = 10$, 20, 30 and 40°, the predicted modifications of the maximum crest height due to the set-down or set-up of the wave-averaged free surface are −0.22, −0.12, 0.00 and +0.13 m respectively. The contributions from the frequency-sum components, not considered explicitly herein, but given in appendix E, would be +1.4, +1.2, +1.0 and +0.83 m, giving a total crest modification at second order of +1.1, +1.1, +1.0 and +0.96 m. Unlike the wave-averaged free surface, which is slowly varying in time and slowly varying (set-down) or rapidly varying (set-up) in space, the frequency-sum components are rapidly varying in both space and time (at twice the frequency and wavenumber).

For two identical wave groups with a small degree of individual spreading $\sigma_\theta = 20°$ that cross at angles of 45, 90, 135 and 180° and have a combined linear amplitude of 10 m at the point of crossing, the predicted modifications of the maximum crest height due to set-down or set-up of the wave-averaged free surface are +0.00, +0.27, +0.50 and +0.60 m respectively. The contributions from the frequency-sum components (appendix E) would be +1.0, +0.63, +0.45 and +0.45 m, giving a total crest modification at second order of +1.0, +0.90, +0.96 and +1.1 m. Here, as the crossing angle increases, the contribution from the frequency-sum components decreases by approximately the same amount as the contribution from the set-up increases. In reality, it is likely that crossing waves that result from wind and swell systems will be of different frequencies, which will affect the magnitude of the set-up at large angles. Nevertheless, this study reinforces the notion that the crossing of waves presents a likely scenario for the observation of a large set-up observed under extreme or freak waves in the oceans. The effects of finite water depth of the linear waves ($k_0 d = O(1)$) will act to increase the magnitude of the set-up, which will be considered in future work.

Acknowledgements

The authors would like to thank Dr S. Draycott and Dr T. Davey at the FloWave Ocean Energy Research Facility (FloWave) for their help in planning and carrying out the experiments. The FloWave facility was funded by the UK's Engineering and Physical Sciences Research Council under grant EP/I02932X/1. The first-named author is the recipient of an EPSRC studentship under the DTP.

Supplementary movies

Supplementary movies are available at https://doi.org/10.1017/jfm.2017.774.

Appendix A. Second-order interaction kernels

The interaction kernels for the sum B^+ and difference B^- terms at second order and for general water depth are given by (Dalzell 1999)

$$B^+ = \frac{\omega_n^2 + \omega_m^2}{2g} - \frac{\omega_n \omega_m}{2g}\left(1 - \frac{\cos(\theta_i - \theta_j)}{\tanh(|\boldsymbol{k}_{n,i}|d)\tanh(|\boldsymbol{k}_{m,j}|d)}\right) \times \left(\frac{(\omega_n + \omega_m)^2 + g|\boldsymbol{k}_{n,i} + \boldsymbol{k}_{m,j}|\tanh(|\boldsymbol{k}_{n,i} + \boldsymbol{k}_{m,j}|d)}{C^+(\boldsymbol{k}_{n,i}, \boldsymbol{k}_{m,j}, \omega_n, \omega_m, d)}\right) + \frac{(\omega_n + \omega_m)}{2gC^+(\boldsymbol{k}_{n,i}, \boldsymbol{k}_{m,j}, \omega_n, \omega_m, d)}\left[\frac{\omega_n^3}{\sinh^2(|\boldsymbol{k}_{n,i}|d)} + \frac{\omega_m^3}{\sinh^2(|\boldsymbol{k}_m|d)}\right], \quad \text{(A 1)}$$

$$B^{-} = \frac{\omega_n^2+\omega_m^2}{2g} + \frac{\omega_n\omega_m}{2g}\left(1+\frac{\cos(\theta_i-\theta_j)}{\tanh(|\boldsymbol{k}_{n,i}|d)\tanh(|\boldsymbol{k}_{m,j}|d)}\right) \times \left(\frac{(\omega_n-\omega_m)^2+g|\boldsymbol{k}_{n,i}-\boldsymbol{k}_{m,j}|\tanh(|\boldsymbol{k}_{n,i}-\boldsymbol{k}_{m,j}|d)}{C^{-}(\boldsymbol{k}_{n,i},\boldsymbol{k}_{m,j},\omega_n,\omega_m,d)}\right) + \frac{(\omega_n-\omega_m)}{2gC^{-}(\boldsymbol{k}_{n,i},\boldsymbol{k}_{m,j},\omega_n,\omega_m,d)}\left[\frac{\omega_n^3}{\sinh^2(|\boldsymbol{k}_{n,i}|d)}-\frac{\omega_m^3}{\sinh^2(|\boldsymbol{k}_m|d)}\right], \quad (A\,2)$$

where the coefficients C^{+} and C^{-} are respectively given by

$$C^{+}(\boldsymbol{k}_{n,i},\boldsymbol{k}_{m,j},\omega_n,\omega_m,d) = (\omega_n+\omega_m)^2 - g|\boldsymbol{k}_{n,i}+\boldsymbol{k}_{m,j}|\tanh(|\boldsymbol{k}_{n,i}+\boldsymbol{k}_{m,j}|d) \quad (A\,3)$$

and

$$C^{-}(\boldsymbol{k}_{n,i},\boldsymbol{k}_{m,j},\omega_n,\omega_m,d) = (\omega_n-\omega_m)^2 - g|\boldsymbol{k}_{n,i}-\boldsymbol{k}_{m,j}|\tanh(|\boldsymbol{k}_{n,i}-\boldsymbol{k}_{m,j}|d). \quad (A\,4)$$

Appendix B. Harmonic separation

B.1. *Two-phase harmonic extraction*

Two-phase harmonic extraction through the creation of crest- and trough-focus wave groups η_0 and η_{180} allows for the separation of harmonics of odd and even powers in amplitude (Baldock *et al.* 1996),

$$\eta_{even} = \frac{\eta_0-\eta_{180}}{2} = \eta^{(1,1)}+\eta^{(3,1)}+\eta^{(3,3)}, \quad (B\,1)$$

$$\eta_{odd} = \frac{\eta_0+\eta_{180}}{2} = \eta^{(2,0)}+\eta^{(2,2)}+\eta^{(4,0)}+\eta^{(4,2)}+\eta^{(4,4)}, \quad (B\,2)$$

where in the superscript the first index refers to the power in amplitude and the second to the harmonic. Provided that the groups under consideration are sufficiently narrow-banded, individual harmonic components can then be cleanly extracted through filtering.

B.2. *Four-phase harmonic extraction*

By repeating experiments at two further phase shifts of 90 and 270°, four-phase extraction allows for the following separation of harmonics (Fitzgerald *et al.* 2014):

$$\frac{\eta_0-\tilde{\eta}_{90}-\eta_{180}+\tilde{\eta}_{270}}{4} = \eta^{(1)}+\eta^{(3,1)}, \quad (B\,3)$$

$$\frac{\eta_0-\eta_{90}+\eta_{180}-\eta_{270}}{4} = \eta^{(2,2)}+\eta^{(4,2)}, \quad (B\,4)$$

$$\frac{\eta_0+\tilde{\eta}_{90}-\eta_{180}-\tilde{\eta}_{270}}{4} = \eta^{(3,3)}, \quad (B\,5)$$

$$\frac{\eta_0+\eta_{90}+\eta_{180}+\eta_{270}}{4} = \eta^{(2,0)}+\eta^{(4,0)}+\eta^{(4,4)}, \quad (B\,6)$$

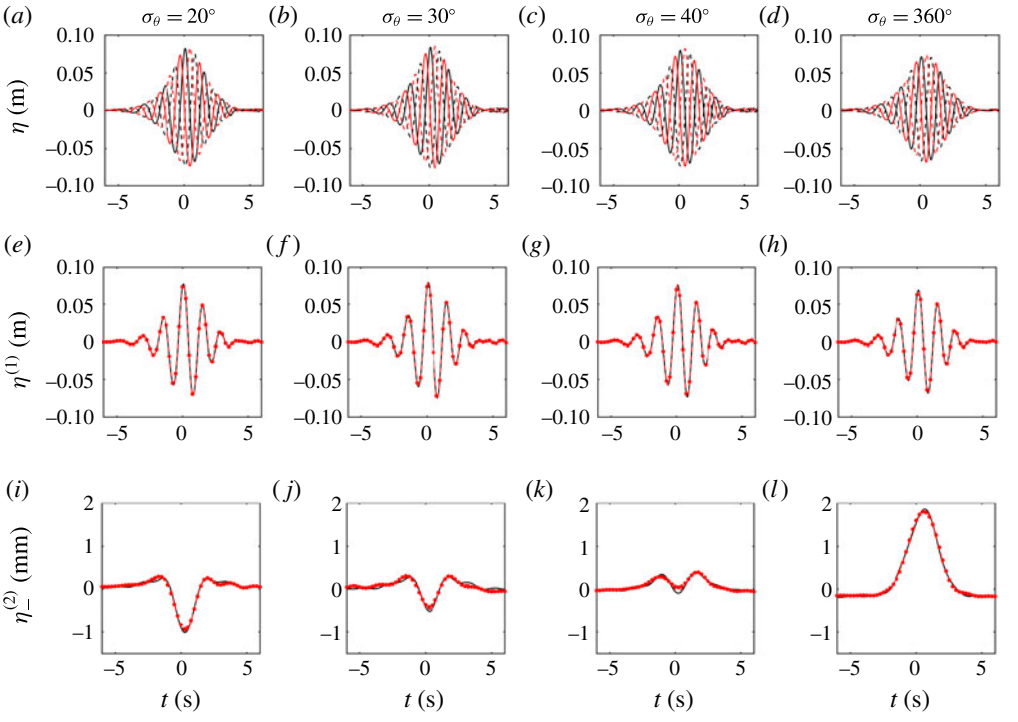

FIGURE 17. (Colour online) Results of four-phase harmonic extraction for degrees of spreading $\sigma_\theta = 20, 30, 40, 360°$: measured time series η_0 (black line), η_{90} (red line), η_{180} (black dashed line) and η_{270} (red dashed line) at the central probe ($x = 0$, $y = 0$) (*a–d*); extracted linear waves $\eta^{(1)}$ (*e–h*); extracted wave-averaged free surface $\eta^{(2)}_-$ (*i–j*). The black lines denote results obtained from the two-phase method and the red dots those from the four-phase method.

where the tilde denotes a Hilbert transform. Second-order sum and difference terms can now be separated without any filtering. To assess both two- and four-phase methods, tests A.3–4 and A.13 are carried out with four phase shifts, as shown in figure 17(*a–d*). The linear and wave-averaged surface elevations extracted using both methods are compared in (*e*)–(*h*) and (*i*)–(*l*) respectively. The results generated by both methods compare very well. Figure 18 displays (log-scaled) amplitude spectra of the extracted harmonic components. Over the range of 0–0.5ω_0, the sum and difference terms are well separated. Hence, both methods produce similar estimates of the wave-averaged surface elevation.

Appendix C. Measurement error and repeatability

C.1. *Residual tank motion (error measure I)*

In order to capture the effect of waves that are not fully absorbed by the wavemakers and remain present in the tank throughout the tests, we measure the variation in the surface elevation after the 10 min of settling time between experiments. Specifically, we define $\Delta\eta_I$ as the difference between the maximum and the minimum surface elevation in the 32 s window before tests. In order to assess the effect of this residual tank motion on the error in the wave-averaged free surface, we apply the same low-pass filter to the residual motion.

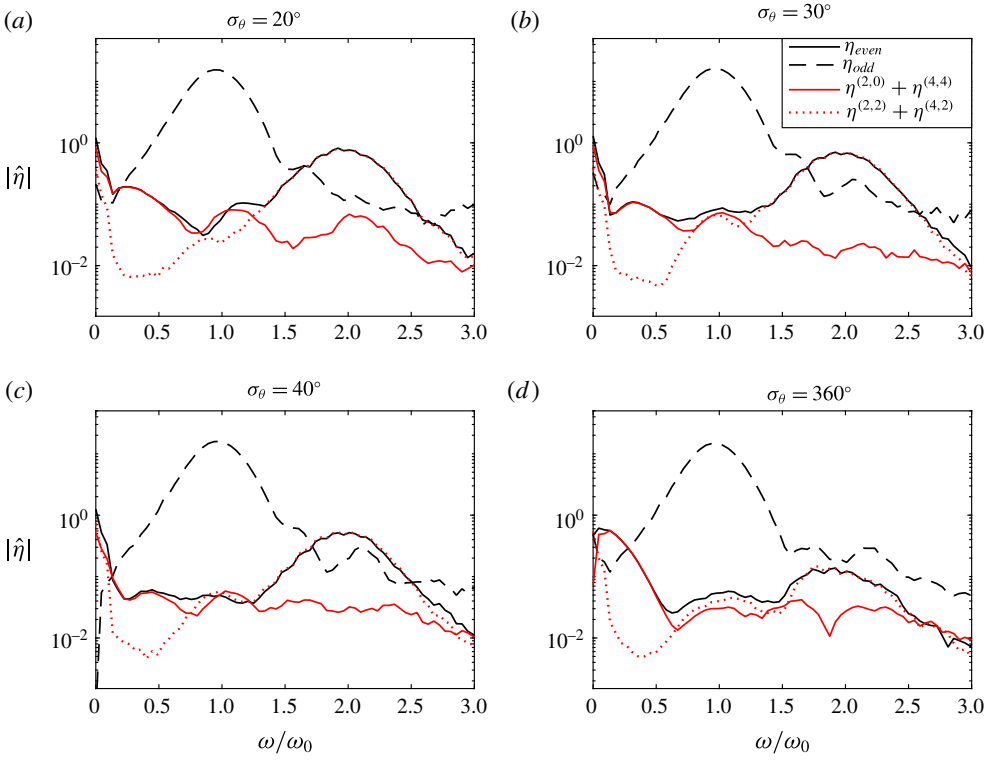

FIGURE 18. (Colour online) Amplitude spectra of extracted harmonic components produced using two- and four-phase extraction methods: two-phase results (black lines) and four-phase results (red lines). The different panels correspond to increasing degrees of input directional spreading $\sigma_\theta = 20, 30, 40, 360°$.

C.2. *Repeatability (error measures II and III)*

To quantify the repeatability of tests (error measure II), $\Delta\eta_{II}$ reports two times the standard deviation of the maximum measured wave-averaged surface amplitude $a^{(2)}_{M-}$ across a number of tests that have been repeated two or three times. Similarly, while performing the spatial measurements, only the mean direction of the wave group is varied. The measurements at the central probe that are thus repeated five times can be used to quantify azimuthal imperfection of the wavemakers and gauge location (error measure III). Two times the standard deviation of the measured wave-averaged surface amplitude $a^{(2)}_{M-}$ for these repeat tests is reported as the error in $\Delta\eta_{III}$.

C.3. *Estimation of directional spreading (error measure IV)*

We estimate the error in the predicted value of the wave-averaged surface amplitude $a^{(2)}_{T-}$ that arises from the estimation of the degree of directional spreading $\sigma^\star_\theta$ from the linearized signal. The estimates of $\sigma^\star_\theta$ in tables 2–3 are obtained from (3.7) using all 14 probes. Estimation of $\sigma^\star_\theta$ using fewer than 14 probes allows for multiple estimates of $\sigma^\star_\theta$ using different combinations of probes. Here, we use combinations of seven of the 14 probes (excluding the central probe). This allows for 1716 (=13!/(7!6!)) estimates of $\sigma^\star_\theta$, from which we can compute a standard deviation $\Delta\sigma^\star_\theta$. To avoid the

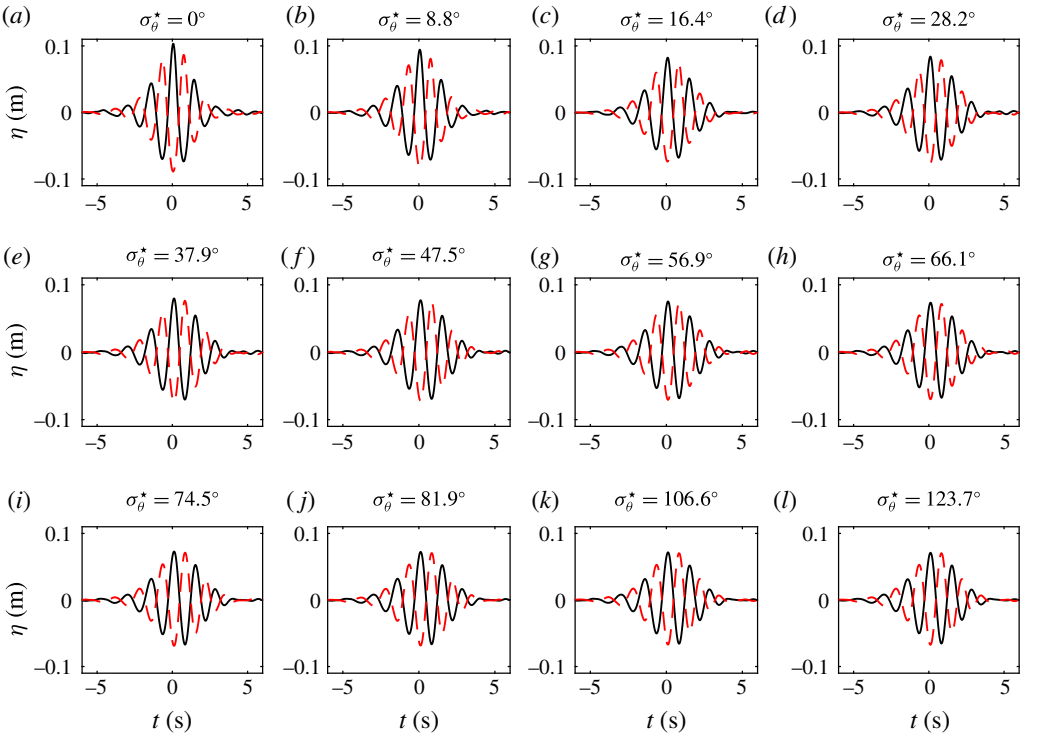

FIGURE 19. (Colour online) Measured time series η at the central probe ($x = 0$, $y = 0$) for the spreading tests (category A), showing crest-focused groups η_0 (black lines) and trough-focused groups η_{180} (red dashed lines) for an input amplitude of $a_0 = 0.1$ m. The different panels correspond to increasing degrees of input spreading $\sigma_\theta = 0$–$180°$, with estimated values $\sigma_\theta^\star$ given in the labels.

time-consuming computation of the wave-averaged free-surface amplitude $a_{T-}^{(2)}$ for all estimates of $\sigma_\theta^\star$, we compute upper and lower bounds of $a_{T-}^{(2)}$ using $\sigma_\theta^\star - 2\Delta\sigma_\theta^\star$ and $\sigma_\theta^\star + 2\Delta\sigma_\theta^\star$ and report the average difference with the mean as our error measure $\Delta\eta_{IV}$. It should be noted that the means of the resampled spreading estimates agree with the value obtained using all 14 probes, demonstrating that our estimator (3.7) is unbiased.

C.4. *Wave gauge calibration (error measure V)*

Finally, the error associated with wave gauge calibration is calculated. The gauges are calibrated by positioning them at known heights in still water and fitting a linear relationship to the resulting measured voltage. Two times the standard deviation of the predicted values of height z is taken as the calibration error $\Delta\eta_V$.

Appendix D. Measured time series

The raw data measured at the central probe for the spreading tests (category A) are presented in figures 19 and 20 and for the crossing tests (category B) in figure 21. Both crest- and trough-focused repeat experiments are shown. In general, the experiments exhibit good focusing, with maxima occurring at $t = 0$, and display horizontal symmetry. However, for the long-crested increased-amplitude wave groups

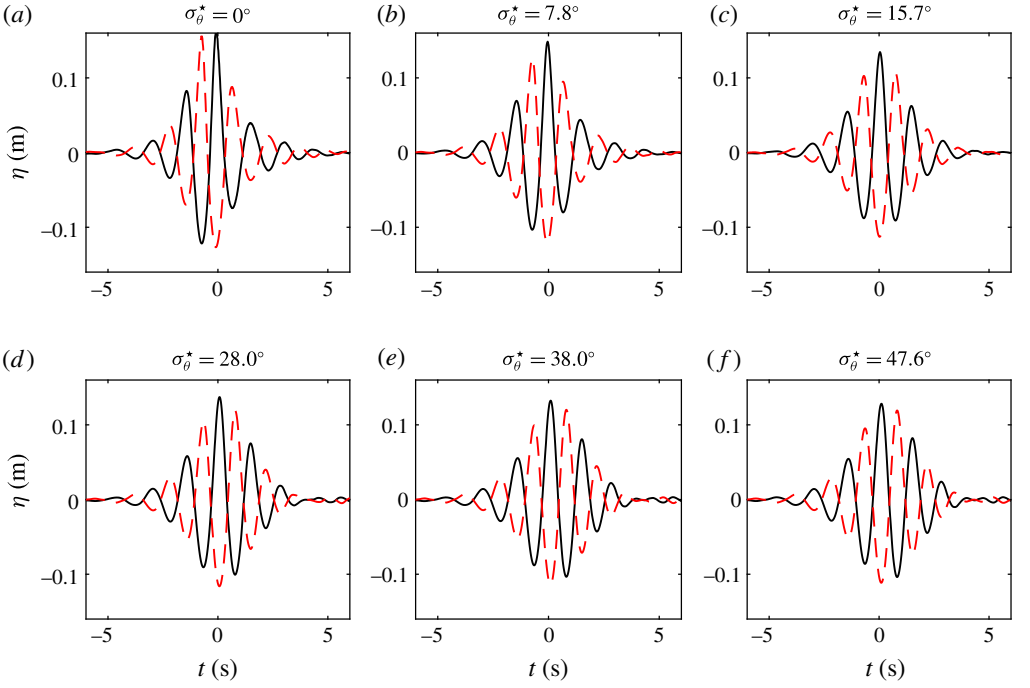

FIGURE 20. (Colour online) Measured time series η at the central probe ($x = 0$, $y = 0$) for the spreading tests (category A), showing crest-focused groups η_0 (black lines) and trough-focused groups η_{180} (red dashed lines) for an input amplitude of $a_0 = 0.15$ m. The different panels correspond to increasing degrees of input spreading $\sigma_\theta = 0$–$50°$, with estimated values $\sigma_\theta^\star$ given in the labels.

in figure 20, the groups exhibit horizontal asymmetry. Here, the dispersion of the free waves is affected by cubic nonlinearity, shifting the location at which the waves focus, as also observed by Taklo *et al.* (2017), among others. As discussed in § 3.3, this will not affect the extraction of the measured wave-averaged surface elevation, but will introduce a phase shift.

Appendix E. Frequency-sum components

As well as the wave-averaged surface elevation, the second-order frequency-sum components $\eta_+^{(2)}$ corresponding to the linear signal (2.20) may be calculated (Dalzell 1999),

$$\eta_+^{(2)} = \sum_{n=1}^{N_\omega}\sum_{m=1}^{N_\omega}\sum_{i=1}^{N_\theta}\sum_{j=1}^{N_\theta} \Omega(\theta_i)\Omega(\theta_j)\hat{\eta}_n\hat{\eta}_m B^+(\boldsymbol{k}_{n,i}, \boldsymbol{k}_{m,j}, \omega_n, \omega_m, d)\cos(\varphi_{n,i} + \varphi_{m,j}), \quad \text{(E 1)}$$

where the interaction kernel B^+ is given in appendix A.

For a single wave group, figure 22 compares the measured amplitude of the frequency-sum components $a_+^{(2)}$ with those predicted for a single Gaussian wave group (category A) as a function of the spreading. Here, $a_+^{(2)}$ is calculated using the wave envelope in order to circumvent the phase-sensitive nature of these high-frequency

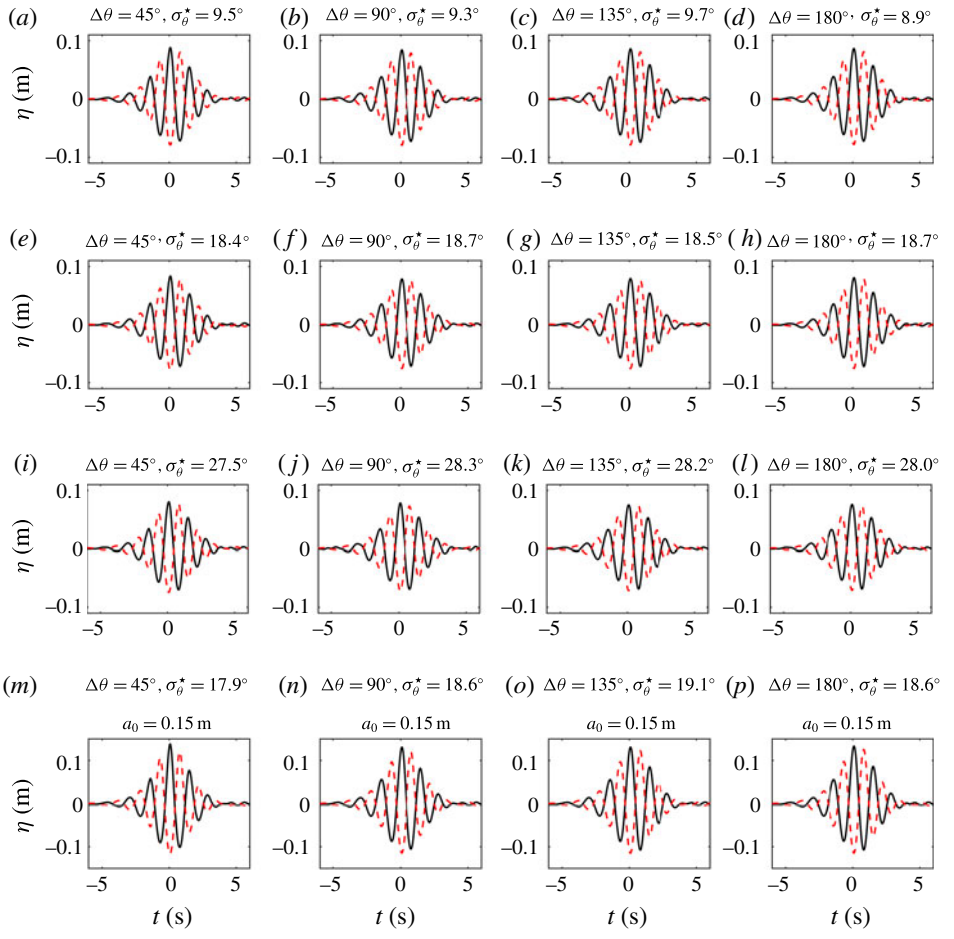

FIGURE 21. (Colour online) Measured time series η at the central probe ($x = 0$, $y = 0$) for the crossing tests (category B), showing crest-focused groups η_0 (black lines) and trough-focused groups η_{180} (red dashed lines) for an input amplitude of $a_0 = 0.1$ m, for increasing values of the crossing angle $\Delta\theta = 0$–$180°$ and increasing degree of input spreading $\sigma_\theta = 10, 20, 30°$ (*a–d*,*e–h*,*i–l*), with estimated values $\sigma_\theta^\star$ given in the labels; (*m–p*) correspond to increased-amplitude experiments at $a_0 = 0.15$ m.

waves. As the frequency-sum components are composed of high-frequency waves, the location of the maximum is more sensitive to the phase. At low values of spreading, the sum waves are larger than expected for a Gaussian wavepacket, which could be the result of unabsorbed reflections or a non-Gaussian spectral tail.

For two crossing groups, figure 23 shows the measured amplitude of the frequency-sum components $a_+^{(2)}$ as a function of the crossing angle (category B). As with the spreading tests, the measured values $a_{M+}^{(2)}$ are larger than predicted for Gaussian wavepackets at low crossing angles only. For larger crossing angles, the theory and the experiments agree well. Panel (*a*) compares the predicted amplitudes of the frequency-sum components $a_{T+}^{(2)}$ with the measured ones $a_{M+}^{(2)}$, showing good agreement.

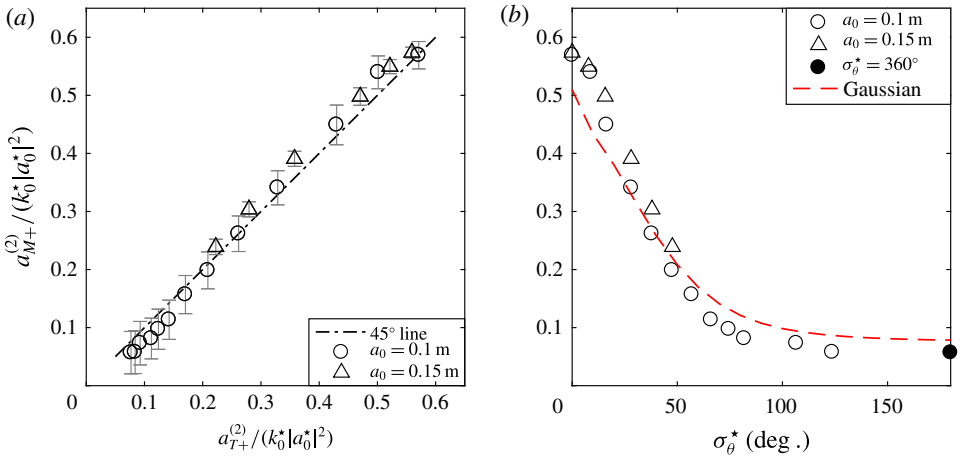

FIGURE 22. (Colour online) The amplitude of the second-order frequency-sum components at the central probe ($x = 0$, $y = 0$) for the spreading tests (category A). (*a*) The measured amplitude $a_{M+}^{(2)}$ as a function of the theoretical prediction $a_{T+}^{(2)}$, with error bars shown in grey (see § 3.6 and appendix C for details), and (*b*) the measured amplitude $a_{M+}^{(2)}$ as a function of the estimated degree of spreading $\sigma_\theta^\star$.

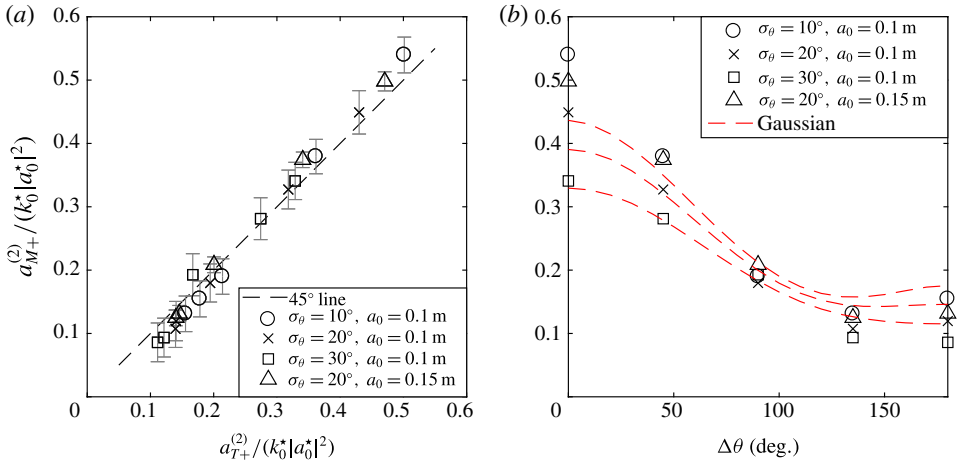

FIGURE 23. (Colour online) The amplitude of the second-order frequency-sum components at the central probe ($x = 0$, $y = 0$) for the crossing tests (category B). (*a*) The measured amplitude $a_{M+}^{(2)}$ as a function of the theoretical prediction $a_{T+}^{(2)}$, with error bars shown in grey (see § 3.6 and appendix C for details), and (*b*) the measured amplitude $a_{M+}^{(2)}$ as a function of the crossing angle $\Delta\theta$.

REFERENCES

ADCOCK, T. A. A. & TAYLOR, P. H. 2009 Estimating ocean wave directional spreading from an Eulerian surface elevation time history. *Proc. R. Soc. Lond.* A **465**, 3361–3381.

ADCOCK, T. A. A. & TAYLOR, P. H. 2014 The physics of anomalous ('rogue') ocean waves. *Rep. Prog. Phys.* **465**, 3361–3381.

ADCOCK, T. A. A., TAYLOR, P. H., YAN, S., MA, Q. W. & JANSSEN, P. A. E. M. 2011 Did the Draupner wave occur in a crossing sea? *Proc. R. Soc. Lond.* A **467**, 3004–3021.

BALDOCK, T. E., SWAN, C. & TAYLOR, P. H. 1996 A laboratory study of nonlinear surface waves on water. *Phil. Trans. R. Soc. Lond.* A **354**, 649–676.

BENOIT, M., FRIGAARD, P. & SCHÄFFER, H. A. 1997 Analysing multidirectional wave spectra: a tentative classification of available methods. In *Proceedings IAHR Seminar on Multidirectional Waves and their Interaction with Structures*, pp. 131–154. International Association for Hydro-Environment Engineering and Research.

VAN DEN BREMER, T. S. & TAYLOR, P. H. 2015 Estimates of Lagrangian transport by wave groups: the effects of finite depth and directionality. *J. Geophys. Res.* **120** (4), 2701–2722.

VAN DEN BREMER, T. S. & TAYLOR, P. H. 2016 Lagrangian transport for two-dimensional deep-water surface gravity wave groups. *Proc. R. Soc. Lond.* A **472**, 20160159.

BÜHLER, O. & MCINTYRE, M. E. 2003 Remote recoil: a new wave-mean interaction effect. *J. Fluid Mech.* **492**, 207–230.

CAVALERI, L., BARBARIOL, L. F., BENETAZZO, A., BERTOTTI, L., BIDLOT, J.-R., JANSSEN, P. A. E. M. & WEDI, N. 2016 The Draupner wave: a fresh look and the emerging view. *J. Geophys. Res.-Oceans* **128**, 6061–6075.

DALZELL, J. F. 1999 A note on finite depth second-order wave–wave interactions. *Appl. Ocean Res.* **21**, 105–111.

DAVEY, A. & STEWARTSON, K. 1974 On three-dimensional packets of surface waves. *Proc. R. Soc. Lond.* A **338**, 101–110.

DYSTHE, K. B. 1979 Note on a modification to the nonlinear Schrodinger equation for application to deep water waves. *Proc. R. Soc. Lond.* A **369**, 105–114.

DYSTHE, K. B., MÜLLER, P. & KROGSTAD, H. E. 2008 Oceanic rogue waves. *Annu. Rev. Fluid Mech.* **40**, 287–310.

FEDELE, F., BRENNAN, J., DE LEÓN, S. P., DUDLEY, J. & DIAS, F. 2016 Real world ocean rogue waves explained without the modulational instability. *Sci. Rep.* **6**, 27715.

FITZGERALD, C. J., TAYLOR, P. H., EATOCK TAYLOR, R., GRICE, J. & ZANG, J. 2014 Phase manipulation and the harmonic components of ringing forces on a surface-piercing column. *Proc. R. Soc. Lond.* A **470**, 20130847.

FORRISTALL, G. Z. 2000 Wave crest distributions: observations and second-order theory. *J. Phys. Oceanogr.* **30**, 1931–1943.

GIBBS, R. H. & TAYLOR, P. H. 2005 Formation of walls of water in fully nonlinear simulations. *Appl. Ocean Res.* **27**, 142–157.

HASSELMANN, K. 1962 On the non-linear energy transfer in a gravity-wave spectrum part 1. General theory. *J. Fluid Mech.* **12**, 481–500.

HERBERS, T. H. C., ELGAR, S. & GUZA, R. T. 1994 Infragravity-frequency (0.005–0.05 Hz) motions on the shelf. Part I: forced waves. *J. Phys. Oceanogr.* **24**, 917–927.

HERBERS, T. H. C. & JANSSEN, T. T. 2016 Lagrangian surface wave motion and Stokes drift fluctuations. *J. Phys. Oceanogr.* **46**, 1009–1021.

INGRAM, D., WALLACE, R., ROBINSON, A. & BRYDEN, I. 2014 The design and commissioning of the first, circular, combined current and wave test basin. In *OCEANS 2014 – Taipei*, pp. 1–7. The Institute of Electrical and Electronics Engineers.

JOHANNESSEN, T. B. & SWAN, C. 2001 A laboratory study of the focusing of transient and directionally spread surface water waves. *Proc. R. Soc. Lond.* A **457**, 971–1006.

KHARIF, C. & PELINOVSKY, E. 2003 Physical mechanisms of the rogue wave phenomenon. *Eur. J. Mech. (B/Fluids)* **22**, 603–634.

KROGSTAD, H. E. 1988 Maximum likelihood estimation of ocean wave spectra from general arrays of wave gauges. *Model. Identif. Control* **9**, 81–97.

LAKE, B. M., YUEN, H. C., RUNGALDIER, H. & FERGUSON, W. E. 1977 Nonlinear deep-water waves: theory and experiment. Part 2. Evolution of a continuous wave train. *J. Fluid Mech.* **83**, 49–74.

LONGUET-HIGGINS, M. S. & STEWART, R. W. 1962 Radiation stress and mass transport in gravity waves, with applications to 'surf beats'. *J. Fluid Mech.* **13**, 481–504.

LONGUET-HIGGINS, M. S. & STEWART, R. W. 1964 Radiation stresses in water waves; a physical discussion, with applications. *Deep-Sea Res.* **2**, 529–562.

MAI, T., GREAVES, D. M., RABY, A. C. & TAYLOR, P. H. 2016 Physical modelling of wave scattering around fixed FPSO-shaped bodies. *Appl. Ocean Res.* **61**, 115–129.

MCINTYRE, M. E. 1981 On the wave momentum myth. *J. Fluid Mech.* **106**, 331–347.

OKIHIRO, M., GUZA, R. T. & SEYMOUR, R. J. 1992 Bound infra-gravity waves. *J. Geophys. Res.* **97**, 453–469.

ONORATO, M., CAVALERI, L., FOUQUES, S., GRAMSTAD, O., JANSSEN, P. A. E. M., MONBALIU, J., OSBORNE, A. R., PAKOZDI, C., SERIO, M. & STANSBERG, C. T. 2009 Statistical properties of mechanically generated surface gravity waves: a laboratory experiment in a three-dimensional wave basin. *J. Fluid Mech.* **627**, 235–257.

ONORATO, M., OSBORNE, A. R. & SERIO, M. 2006 Modulational instability in crossing sea states: a possible mechanism for the formation of freak waves. *Phys. Rev. Lett.* **96**, 014503.

ONORATO, M., RESIDORI, S., BORTOLOZZO, U., MONTINA, A. & ARECCHI, F. T. 2013 Rogue waves and their generating mechanisms in different physical contexts. *Phys. Rep.* **528**, 47–89.

PELLET, L., CHRISTODOULIDES, P., DONNE, S., BEAN, C. J. & DIAS, F. 2017 Pressure induced by the interaction of water waves with nearly equal frequencies and nearly opposite directions. *Theor. Appl. Mech. Lett*.

SHARMA, J. N. & DEAN, R. G. 1981 Second-order directional seas and associated wave forces. *Soc. Petrol. Engng J.* **21**, 129–140.

STOKES, G. G. 1847 On the theory of oscillatory waves. *Trans. Camb. Phil. Soc.* **8**, 441–455.

TAKLO, T. M. A., TRULSEN, K., KROGSTAD, H. E. & BORGE, J. C. N. 2017 On dispersion of directional surface gravity waves. *J. Fluid Mech.* **812**, 681–697.

TIAN, Z., PERLIN, M. & CHOI, W. 2011 Frequency spectra evolution of two-dimensional focusing wave groups in finite depth water. *J. Fluid Mech.* **688**, 169–194.

TOFFOLI, A., BITNER-GREGERSEN, E. M., OSBORNE, A. R., SERIO, M., MONBALIU, J. & ONORATO, M. 2011 Extreme waves in random crossing seas: laboratory experiments and numerical simulations. *Geophys. Res. Lett.* **38**, L06605.

TOFFOLI, A., GRAMSTAD, O., MONBALIU, J., TRULSEN, K., BITNER-GREGERSEN, E. M. & ONORATO, M. 2010 Evolution of weakly nonlinear random directional waves: laboratory experiments and numerical simulations. *J. Fluid Mech.* **664**, 313–336.

TOFFOLI, A., MONBALIU, J., ONORATO, M., OSBORNE, A. R., BABANIN, A. V. & BITNER-GREGERSEN, E. M. 2007 Second-order theory and setup in surface gravity waves: a comparison with experimental data. *J. Phys. Oceanogr.* **37**, 2726–2739.

TOFFOLI, A., ONORATO, M. & MONBALIU, J. 2006 Wave statistics in unimodal and bimodal seas from a second-order model. *Eur. J. Mech. (B/Fluids)* **25** (5), 649–661.

WALKER, D. A. G., TAYLOR, P. H. & EATOCK TAYLOR, R. 2004 The shape of large surface waves on the open sea and the Draupner New Year wave. *Appl. Ocean Res.* **26**, 73–83.

ZHAO, W., WOLGAMOT, H. A., TAYLOR, P. H. & EATOCK TAYLOR, R. 2017 Gap resonance and higher harmonics driven by focused transient wave groups. *J. Fluid Mech.* **812**, 905–939.